

Continuous sensing of IFN α by hepatic endothelial cells shapes a vascular antimetastatic barrier

Ngoc Lan Tran^{1*}, Lorena Maria Ferreira^{1*}, Blanca Alvarez-Moya^{1*}, Valentina Buttiglione¹, Barbara Ferrini¹, Paola Zordan^{1,3}, Andrea Monestiroli¹, Claudio Fagioli¹, Eugenia Bezzechi², Giulia Maria Scotti², Antonio Esposito^{3,4}, Riccardo Leone^{3,4}, Chiara Gnasso^{3,4}, Andrea Brendolan⁵, Luca G. Guidotti^{1,3}, and Giovanni Sitia¹

¹Division of Immunology, Transplantation and Infectious Diseases, IRCCS San Raffaele Scientific Institute, 20132 Milan, Italy

²Center for Omics Sciences, IRCCS San Raffaele Hospital, 20132 Milan, Italy

³Vita-Salute San Raffaele University, 20132 Milan, Italy

⁴Experimental Imaging Center, IRCCS San Raffaele Scientific Institute, 20132 Milan, Italy

⁵Division of Experimental Oncology, IRCCS San Raffaele Scientific Institute, 20132 Milan, Italy

* These authors contributed equally to this work

NL. Tran's present address is University of Geneva, Rue Michel-Servet 1, 1211 Genève 4, Switzerland

V. Buttiglione's present address is Ipsen Spa, Via del Bosco Rinnovato 6, 20090 Assago (MI), Italy

Running title: IFN α shapes a liver vascular antimetastatic barrier

Correspondence:

Giovanni Sitia, Division of Immunology, Transplantation and Infectious Diseases, IRCCS San Raffaele Scientific Institute, Via Olgettina 58, 20132 Milan, Italy

Phone: (+39)0226434956

Fax: (+39)0226436822

Email: sitia.giovanni@hsr.it

ORCID: 0000-0003-1024-9128

Abstract

Hepatic metastases are a poor prognostic factor of colorectal carcinoma (CRC) and new strategies to reduce the risk of liver CRC colonization are highly needed. Herein, we used mouse models of hepatic metastatization to demonstrate that the continuous infusion of therapeutic doses of interferon-alpha (IFN α) controls CRC invasion by acting on hepatic endothelial cells (HECs). Mechanistically, IFN α promoted the development of a vascular antimetastatic niche characterized by liver sinusoidal endothelial cells (LSECs) defenestration extracellular matrix and glycocalyx deposition, thus strengthening the liver vascular barrier impairing CRC trans-sinusoidal migration, without requiring a direct action on tumor cells, hepatic stellate cells, hepatocytes, or liver dendritic cells (DCs), Kupffer cells (KCs) and liver capsular macrophages (LCMs). Moreover, IFN α endowed LSECs with efficient cross-priming potential that, along with the early intravascular tumor burden reduction, supported the generation of antitumor CD8⁺ T cells and ultimately led to the establishment of a protective long-term memory T cell response. These findings provide a rationale for the use of continuous IFN α therapy in perioperative settings to reduce CRC metastatic spreading to the liver.

Keywords: Liver metastases/ HECs/ LSECs/ interferon-alpha/ cross-priming/ colorectal cancer.

Introduction

Colorectal cancer (CRC) is the third most common cancer and the second leading cause of cancer-related death worldwide (Sung *et al*, 2021). Surgical resection of the primary CRC tumor is the mainstay of treatment (Argiles *et al*, 2020; Cunningham *et al*, 2010; Seo *et al*, 2013); unfortunately, up to 50% of these patients - despite chemotherapy and targeted adjuvant therapies - often develop life-threatening liver metastatic disease in the following years (Argiles *et al*, 2020; Sargent *et al*, 2009). While the overall benefit of surgery is well established (Seo *et al*, 2013), it has been also proposed that this procedure may foster liver metastases by increasing the dissemination of CRC cells into the portal circulation (Chow & Chok, 2019; Deneve *et al*, 2013), enhancing the adhesion of CRC cells to the liver endothelium (Chambers *et al*, 2002; Gul *et al*, 2011) or promoting transient immunosuppression awakening dormant intrahepatic micrometastases (Ananth *et al*, 2016).

Accordingly, there is growing recognition that the use of perioperative immunotherapies in CRC patients undergoing surgical resection may represent a unique treatment window to prevent metastatic colonization and control minimal residual disease (Badia-Ramentol *et al*, 2021; Bakos *et al*, 2018; Horowitz *et al*, 2015). In this context, interferon-alpha (IFN α), a pleiotropic cytokine with multiple antitumor effects such as the direct inhibition of cancer cell growth and angiogenesis (Indraccolo, 2010), the sustained upregulation of major histocompatibility complexes (Gessani *et al*, 2014) and the induction of innate and adaptive antitumor immune responses (Aichele *et al*, 2006; Curtsinger *et al*, 2007; Fuertes *et al*, 2013), has been used as adjuvant immunotherapy in various solid cancers such as renal cell carcinoma (Flanigan *et al*, 2001), melanoma (Lens & Dawes, 2002) and colorectal cancer (Kohne *et al*, 1997; Link *et al*, 2005). Unfortunately, systemic administration of IFN α has shown limited clinical efficacy, likely due to its short plasma half-life (~1 hour) (Bocci, 1994) and the use of high and pulsed doses, which often resulted in systemic side effects

(Weber *et al*, 2015). To overcome these limitations, several strategies to prolong IFN α half-life and target the tumor microenvironment have been tested (Fioravanti *et al*, 2011; Herndon *et al*, 2012; Jeon *et al*, 2013; Li *et al*, 2017; Liang *et al*, 2018; Yang *et al*, 2014), including a preclinical gene/cell therapy approach that can deliver constant amounts of IFN α into the liver to significantly curb CRC metastatic growth (Catarinella *et al*, 2016).

Herein, we adopted a continuous intraperitoneal (IP) IFN α delivery strategy to show that steady and tolerable IFN α doses reduce liver CRC metastatic spreading and improves survival in several CRC mouse models. Our results showed that the antimetastatic effects of IFN α rely neither on the direct inhibition of tumor cell proliferation nor on the indirect stimulation of hepatocytes, hepatic stellate cells, liver DCs, Kupffer cells (KCs) and liver capsular macrophages (LCMs). Rather, the results identify HECs, including LSECs, as key mediators of IFN α -dependent anti-tumor activities that involve the impairment of CRC trans-sinusoidal migration and the development of long-term anti-tumor CD8⁺ T cell immunity.

Results

Selection of the optimal IFN α dosing regimen

To avoid well-known toxicities, especially myelotoxicity, caused by high IFN α doses (Weber *et al*, 2015) and to define a delivery strategy providing prolonged and non-fluctuating IFN α levels in blood and tissues, normal inbred mice were implanted intraperitoneally with mini-osmotic pumps (MOP) constantly releasing different rates (i.e. 50 ng/day, 150 ng/day, or 1050 ng/day) of recombinant mouse IFN α 1 (termed IFN α from now on) over time. Serum IFN α levels peaked at day 2 after MOP implantation and relative IFN α amounts (from ~100 pg/ml to ~1200 pg/ml) reflected the different MOP loading doses (Fig 1A). Serum IFN α levels decreased, albeit not uniformly, at days 5 and 7 post implantation (Fig 1A), mirroring the pharmacokinetic-pharmacodynamic (PK-PD) behavior of other long-lasting formulations of

IFN α (Jeon *et al.*, 2013). A reduction in circulating white blood cells (WBCs) but not in platelet (PLT) counts or hematocrit (HCT) was detected only with the highest dose (Fig 1B and S1A,B). Looking at liver toxicity, we observed no increases in serum alanine aminotransferase (sALT) at all tested doses and time points (Fig S1C) and no abnormal changes in liver morphology at autopsy (Fig S1D). Looking at the intrahepatic induction of the interferon-stimulated gene (ISG) *Irf7* (Cheon *et al.*, 2014) at day 7, we observed a proportional dose response, with a six-fold increase in *Irf7* expression at the 150 ng/day dosing regimen (Fig 1C). Notably, this increase paralleled the increase that we previously documented to be associated with protection against liver CRC colonization following a gene/cell therapy based IFN α delivery strategy (Catarinella *et al.*, 2016). Lack of bone marrow and liver toxicity, proper induction of hepatic *Irf7* expression and maintained responsiveness of hepatic liver cells to IFN α (Fig S1E) prompted us to select the 150 ng/day dosing regimen for follow-up investigations.

Continuous IFN α administration reduces liver CRC metastatic burden and improves survival

We next tested the ability of continuous IFN α administration (150 ng/day for 28 days) to reduce CRC metastatic growth in the liver. Groups of H-2^{bxd} F1 hybrids of C57BL/6 x BALB/c (CB6) mice were implanted with either control MOP-NaCl (termed NaCl) or MOP-IFN α (termed IFN α) (Fig 2A). Seven days later, a time frame compatible with the perioperative period in humans (Horowitz *et al.*, 2015), CB6 mice were intrasplenically challenged with either the immunogenic microsatellite instable (MSI) MC38 CRC cell line (Efremova *et al.*, 2018; Rosenberg *et al.*, 1986) or the poorly immunogenic microsatellite stable (MSS) CT26 CRC cell line (Brattain *et al.*, 1980; Efremova *et al.*, 2018). Rapid removal of the spleen after CRC cell injection was implemented to avoid intrasplenic tumor growth (Catarinella *et al.*, 2016). Each CRC cell line was injected at doses known to induce similar survival rates in

age- and sex-matched CB6 recipients that, carrying hybrid H-2^{bxd} alleles, are immunologically permissive to both MC38 and CT26 cells (Catarinella *et al.*, 2016). After treatment initiation, well-tolerated serum IFN α levels of ~300 pg/ml at day 2 and ~100 pg/ml thereafter were observed (Fig 2B and Fig S2A,B), which subsequently declined to undetectable levels. The intrahepatic expression of *Irf7* monitored at day 21 after continuous IFN α therapy (Fig S2C,D) was like that observed earlier at day 7 (Fig 1C). Magnetic resonance imaging (MRI)-based longitudinal analyses - in MC38- (Fig 2C and Fig S2E) or CT26-challenged (Fig 2D and Fig S2F) animals - revealed that 100% of NaCl-treated mice (Fig 2E,F) develop multiple metastatic tumor lesions by days 21 and 28 after challenge and no mice displayed detectable tumors in other organs. Liver lesions increased in volume afterwards, ultimately resulting in imposed humane euthanization of both MC38 (Fig S2I) or CT26 (Fig S2J) tumor carriers in the intervening weeks. Conversely, 45% and 66% of IFN α -treated mice challenged with MC38 or CT26 cells, respectively, showed absence of liver metastases throughout the entire duration of the experiment (Fig 2E,F). All the remaining mice scoring disease-positive at days 21 and 28 displayed lesions that were reduced in number and size when compared to those detected in NaCl-treated counterparts (Fig S2G,J). Of note, metastatic lesions eventually regressed and achieved complete remission by day 50 in approximately 33% of IFN α -treated mice that were challenged with MC38 cells and scored disease-positive at day 21 (Fig 2C,E and Fig S2E), whereas none of the few CT26-challenged mice scoring disease-positive at day 21 survived long-term (Fig 2D,F and Fig S2F), with tumors confined only to the liver. Continuous IFN α administration also improved survival, with similar rates for both MC38- and CT26-challenged mice (Fig 2G,H). These results indicate that the continuous IFN α administration safely and efficiently limits the liver metastatic colonization of CRC cell lines intrinsically carrying different immunogenic or genetic properties.

Continuous IFN α administration prevents spontaneous hepatic colonization of orthotopically implanted CT26^{LM3} cells

To confirm the above-mentioned results in a different metastatic setting, we developed an orthotopic CRC model of liver metastases by implanting invasive CRC cells into the mouse cecal wall. As previously reported (Zhang *et al*, 2013), invasive CRC cells were generated by serial intracecal injections of the parental CT26 cells into CB6 mice (Fig S3A). The percentage of metastatic livers in intracecally implanted mice significantly increased as CT26 cells were passaged, with an almost 100% of animals bearing multiple liver metastases after 3 rounds of *in vivo* selection (Fig S3B-D). Three-time passaged cells (termed CT26^{LM3}) were then orthotopically implanted in the cecal wall of CB6 mice and 7 days later the animals were treated with either NaCl or IFN α (Fig 3A).

Consistent with our previous results (Fig 2B), serum IFN α levels peaked at day 2 after MOP implantation (Fig 3B), without causing myelotoxicity (Fig 3C), and MRI analyses performed 14 days later revealed that continuous IFN α therapy did not alter the growth of primary intracecal tumors (Fig 3D,E), while IFN α treatment significantly reduced both number and size of hepatic lesions (Fig 3D,F) with 60% of mice spared from metastatic lesions (Fig 3H). The primary intracecal tumors (Fig S4A) and liver metastases (Fig 3G) detected after orthotopic implantation of CT26^{LM3} cells were also characterized by immunohistochemistry (IHC). This analysis showed that primary intracecal tumors and liver metastatic lesions of NaCl-treated control mice were highly proliferative (as denoted by Ki67 positivity), exhibited marked signs of angiogenesis (as denoted by CD34 staining) and, accordingly with previous reports (Catarinella *et al.*, 2016; Tauriello *et al*, 2018), were devoted of F4/80⁺ resident macrophages and CD3⁺ T cells (Fig 3G,H). Similar results were also observed in IFN α -treated primary intracecal tumors (Fig S4A,B). The absence of liver metastases in the majority of IFN α -treated mice is reflected by a reduced Ki67 or CD34 staining and an apparently normal distribution of F4/80⁺ macrophages and CD3⁺ T cells (Fig 3G,H). The few

small hepatic lesions detected in 40% of mice continuously treated with IFN α (Fig 3H and S4C,D) did not show differences in Ki67 positivity, CD34 staining or amount of F4/80⁺ resident macrophages and CD3⁺ T cells in relation to NaCl-treated mice (Fig S4C,D), consistent with the notion that CRC tumors may deregulate the *Ifnar1* receptor and, thus, become refractory to IFN α therapy (Boukhaled *et al*, 2021; Katlinski *et al*, 2017). Altogether, these results indicate that continuous IFN α therapy does not significantly alter the growth of primary established CRC tumors but reduces the liver metastatic potential of invasive CRC cells emerging from the cecum.

HECs mediate the anti-metastatic activity of IFN α

As the *Ifnar1* surface receptor subunit is necessary to mediate the pleiotropic anti-tumor properties of IFN α (Cheon *et al.*, 2014), we deleted this molecule from CRC cells and from hepatic parenchymal and non-parenchymal cells to identify the mechanism of action (MoA) of continuous IFN α administration in our *in vivo* system. We restricted these studies to MC38 CRC cells because the genetic background of the mouse models did not allow us to use CT26 CRC MHC-I mismatched cell lines in C57BL/6 recipients. We also adopted a new seeding approach that - involving the injection of CRC cells through the superior mesenteric vein - potentially avoids immune deregulations linked to the splenectomy procedure. Seven days after NaCl or IFN α administration, C57BL/6 mice were challenged with wild-type MC38 cells or with MC38 cells that were CRISPR-Cas9-edited to lack a functional *Ifnar1* receptor (MC38^{*Ifnar1* KO}). To this end, MC38-edited clones showed mismatches in a T7E1 assay and clone C8 (MC38^{C8}) carrying *Ifnar1* deleting mutations failed to express *Irf7* upon *in vitro* IFN α stimulation (Fig S5A-C).

MRI analysis at day 21 after CRC challenge revealed that, in comparison with liver metastases observed in NaCl-treated controls, the lesions produced by MC38- or MC38^{*Ifnar1* KO} cells in IFN α -treated mice were similarly reduced in number and size (Fig

4A,C-D) and this resulted in comparable mouse survival rates (Fig 4E) in the absence of apparent myelotoxicity (Fig S6A). These data support the hypothesis that in our experimental setting the continuous IFN α administration has no direct antiproliferative activity towards CRC cells consistent with our previous reported data (Fig S5A-C) (Catarinella *et al.*, 2016).

Next, we crossed *Ifnar1*-floxed mice (termed *Ifnar1^{fl/fl}*) (Prigge *et al.*, 2015) with transgenic mice selectively expressing Cre recombinase in parenchymal and non-parenchymal liver cells (Gerl *et al.*, 2015; Postic *et al.*, 1999; Wang *et al.*, 2010) (Fig S5D). Cell type-specific recombination was confirmed by crossing each parental mouse line with Rosa26-ZsGreen reporter mice. Note that by crossing the parental Cre-expressing lines with Rosa26-ZsGreen reporter mice (Madisen *et al.*, 2010) the resultant mice showed specific recombination in most hepatocytes (identified by morphology), and liver fibroblast (GFP⁺/PDGFR β ⁺), with about 98.2 \pm 0.72% hepatic stellate cells that co-expressed GFP⁺ and PDGFR β ⁺ signals (Fig S5E,F). Similarly, hepatic DCs (GFP⁺/CD11c⁺) had 94.17 \pm 2.16% colocalization with GFP, while the colocalization percentage of F4/80⁺ KCs or LCMs (GFP⁺/F4/80⁺) was 78.14 \pm 5.03% (Fig S5E,F) (Bleriot & Ginhoux, 2019; Karmaus & Chi, 2014; Madisen *et al.*, 2010). Finally, HECs, including LSECs, (GFP⁺/CD31⁺) showed 85.3 \pm 5.03% colocalization (Fig S5E,F), with no expression of GFP signals in cells other than CD31⁺. *Ifnar1^{fl/fl}* control mice and mice lacking *Ifnar1* in hepatocytes (termed Alb^{*Ifnar1*-KO}), hepatic stellate cells (termed PDGFR β ^{*Ifnar1*-KO}), DCs/KCs/LCMs (termed CD11c^{*Ifnar1*-KO}) or Cdh5⁺ endothelial cells (termed VeCad^{*Ifnar1*-KO}) were intrasenterically injected with MC38 cells 7 days after NaCl or IFN α therapy initiation and did not show signs of hematotoxicity during IFN α infusion (Fig S6B). Metastatic growth was assessed by MRI at day 21 (Fig 4B). Loss of *Ifnar1* on hepatocytes, hepatic stellate cells or DCs/KCs/LCMs did not significantly alter the anti-metastatic activity of IFN α treatment (Fig 4C,D and F and Fig S6C). By contrast, the depletion of *Ifnar1* on HECs allowed the lesions to grow undisturbed (Fig 4B). Indeed,

VeCad^{*Ifnar1*^{-KO}} mice treated with either NaCl or IFN α displayed very similar numbers and sizes of hepatic lesions (Fig 4C,D) or survival rates (Fig 4F), indicating that the antimetastatic properties of IFN α requires *Ifnar1* signaling on HECs. VeCad^{*Ifnar1*^{-KO}} mice exhibited increased tumor burden (Fig 4D) and mortality rates (Fig S6D) when compared to NaCl-treated *Ifnar1*^{*fl/fl*} mice, suggesting that hepatic endothelial *Ifnar1* signaling exerts significant anti-tumor activity even in the context of physiologic endogenous intrahepatic levels of type I interferons. Furthermore, histological analysis of hepatic CRC lesions from NaCl- and IFN α -treated VeCad^{*Ifnar1*^{-KO}} mice euthanized at day 21 after MC38 intrasenteric injection indicated that these tumors resembled NaCl-treated *Ifnar1*^{*fl/fl*} lesions, showing signs of angiogenesis (as denoted by CD34 positivity) and similar content of F4/80⁺ macrophages and CD3⁺ T cells within the intrahepatic CRC foci (Fig S7A,B).

Continuous IFN α administration limits trans-sinusoidal migration of CRC cells by strengthening the liver vascular barrier

We next took advantage of fluorescence-based techniques to investigate the initial steps of liver colonization. First, we assessed the intrahepatic localization of GFP-expressing MC38 cells (MC38^{GFP}) (Talamini *et al*, 2021) that were intrasenterically challenged 5 min earlier. Most MC38^{GFP} cells in *Ifnar1*^{*fl/fl*} or VeCad^{*Ifnar1*^{-KO}} mice appeared physically trapped at the beginning of the sinusoidal circulation in both mouse lineages. This was evidenced by the close contact of MC38^{GFP} cells with Lyve1-expressing LSECs in the proximity of the portal tracts (Fig S8A). Further, MC38^{GFP} cells arrested where the sinusoidal diameter (Fig S8B) is smaller than their own ($12 \pm 0.1 \mu\text{m}$), similar to what we previously reported (Catarinella *et al.*, 2016). As the process of trans-sinusoidal migration - a critical limiting step in the metastatic cascade - is known to occur within 24 hours of CRC challenge (Chambers *et al.*, 2002; Valastyan & Weinberg, 2011; Wolf *et al*, 2012), the intrahepatic number and localization of MC38^{GFP} cells were then studied at this time point. Confocal IF quantification

revealed that, compared to NaCl-treated *Ifnar1^{fl/fl}* animals, MC38^{GFP} cells were about ~2-fold less abundant in IFN α -treated *Ifnar1^{fl/fl}* mice and ~3-fold more abundant in VeCad^{*Ifnar1*^{-KO}} mice treated with NaCl or IFN α (Fig 5A top). Moreover, confocal 3D reconstructions of liver sinusoids from IFN α -treated *Ifnar1^{fl/fl}* mice unveiled that by 24 hours most MC38^{GFP} cells localize intravascularly (i.e. they did not invade the liver parenchyma), while in NaCl-treated *Ifnar1^{fl/fl}* controls and in NaCl- or IFN α -treated VeCad^{*Ifnar1*^{-KO}} mice only few MC38^{GFP} cells remain within the liver vasculature (i.e. they invaded the liver parenchyma) (Fig 5A bottom, 5B and Video S1-4). These results indicate that HECs, including LSECs, negatively control trans-sinusoidal CRC migration upon IFN α sensing.

To unravel phenotypic modifications associated with such antitumor function of HECs, including LSECs, the liver microvasculature of NaCl- or IFN α -treated *Ifnar1^{fl/fl}* and VeCad^{*Ifnar1*^{-KO}} mice was analyzed by scanning electron microscopy (SEM) and transmission electron microscopy (TEM). IFN α treatment of *Ifnar1^{fl/fl}* mice significantly decreased the frequency of sinusoidal fenestrae and the overall porosity of LSECs (Fig 5C,D top), while it increased: i) the endothelial thickness (Fig S8D); ii) the space of Disse density (an indirect measure of hepatocyte microvilli density) (Fig S8D) (Gissen & Arias, 2015); iii) the subendothelial deposition of collagen fibrils (Fig S8D) and; iv) the appearance of a basal lamina (Fig 5D bottom and Fig S8D). These results were corroborated by immunofluorescence analysis assessing an enhanced perivascular expression of collagen type IV and laminin (Fig S8E,F), two components of the basal lamina previously shown to form a barrier against tumor cell invasion (Mak & Mei, 2017; Tanjore & Kalluri, 2006). By contrast, IFN α treatment of VeCad^{*Ifnar1*^{-KO}} mice failed to significantly support these changes, leaving the liver microvasculature of these animals highly similar to that of liver metastases-permissive NaCl-treated *Ifnar1^{fl/fl}* controls (Fig 5C,D and Fig S8D-F). Moreover, IFN α treatment of *Ifnar1^{fl/fl}* mice significantly increased the expression of Lyve-1, a marker of

293 hepatic capillarization (Pandey *et al*, 2020; Wohlfeil *et al*, 2019). By contrast, IFN α treatment
 294 of VeCad^{*Ifnar1*^{-KO}} mice showed no effect (Fig S9A,B).

295 Next, we evaluated the status of the vascular glycocalyx (GCX), a fibrous network of
 296 glycoproteins and proteoglycans that lines the LSECs and projects intraluminally (Reitsma
 297 *et al*, 2007). Notably, enhanced GCX deposits can act as a repulsive barrier that prevents
 298 tumor cell interactions with endothelial cells, adhesion molecules or chemokines have been
 299 previously identified as negative correlates of transendothelial migration (Glinskii *et al*, 2005;
 300 Mitchell & King, 2014; Offeddu *et al*, 2021; Wilkinson *et al*, 2020). Continuous IFN α
 301 treatment modified this network as well, increasing its thickness (Fig 5E,F top) and the
 302 expression of one of its major components, the heparan sulfate (HS) (Reitsma *et al.*, 2007)
 303 (Fig 5E,F bottom). Of note, VeCad^{*Ifnar1*^{-KO}} mice displayed reduced GCX thickness
 304 independently of NaCl- or IFN α -treatment (Fig 5E,F). Additionally, we evaluated the vascular
 305 and perivascular status of cell adhesion molecules such as selectins and integrins, which
 306 have been positively associated with the transendothelial migration of tumor cells (Glinskii
 307 *et al.*, 2005; Wilkinson *et al.*, 2020). The expression of ICAM1, E-selectin (CD62E) (Fig
 308 S8G,H) and the integrins ITGB2 (CD18) or ITGA4 (CD49d) (Fig S8C) was up-regulated in
 309 IFN α -treated *Ifnar1*^{fl/fl} controls, while significantly reduced or attenuated in IFN α -treated
 310 VeCad^{*Ifnar1*^{-KO}} mice. The notion that a more modest upregulation of some these markers
 311 was still evident in the latter mice may reflect the capacity of liver cells other than HECs to
 312 respond to IFN α . Altogether, these results indicate that numerous phenotypic modifications
 313 of the liver microvasculature previously associated with the deficient extravasation of both
 314 normal and transformed cells of different origin (Guidotti *et al*, 2015; Valastyan & Weinberg,
 315 2011) also occur because of continuous IFN α sensing by HECs, including LSECs. Notably,
 316 these microvascular modifications were reverted after the discontinuation of IFN α therapy
 317 with no impact on long-term liver functionality/viability (Fig S9C-I).

318

HECs acquire an antimetastatic transcriptional profile upon continuous IFN α sensing

To confirm the above-mentioned data and to shed new light on the transcriptional changes that HECs adopt to limit CRC trans-sinusoidal migration, we performed RNA-seq analyses on CD31⁺ endothelial cells isolated from the liver of *Ifnar1*^{fl/fl} or VeCad^{*Ifnar1*-KO} mice 7 days after NaCl or IFN α treatment (Fig S10A). Using SEM to assess the % of CD31⁺ cells bearing the typical sinusoidal fenestrae, we determined that our preparations contain ~ 96% of bona-fide LSECs (Fig S10B), consistently to previous reports (Liu *et al*, 2011; Su *et al*, 2021). When compared to HECs isolated from NaCl-treated *Ifnar1*^{fl/fl} mice, HECs derived from IFN α -treated animals of the same lineage showed 381 transcripts that were differentially expressed (Fig 6A). As expected, many of these up-regulated transcripts belonged to the ISG family, including *Irf7*, *Irf9*, *Mx1*, *Mx2*, *Isg15*, *Stat1* and *Oas1* (Fig 6A,B). Pre-ranked gene set enrichment analyses (GSEA) of IFN α -treated LSECs also revealed a significant enrichment of transcripts involved in interferon signaling or in the induction of varying cytokines and chemokines (Fig 6C). Several transcripts related to the ECM/GCX organization or the cell-cell/cell-matrix adhesion pathways were upregulated as well (Fig 6B,D). Of note, the expression of *Itga4* and *Itgb2* - previously shown to be increased by IFN α treatment at the protein level (Fig S8C) - was also enhanced at the transcriptional level (Fig 6B). A similar association did not hold true for *Icam1* and *Sele*, suggesting that the increased protein expression we observed earlier (Fig S8G) occurred independently of transcriptional activity (Fig 6B). Notably, GSEA also identified gene sets involved in the IFN α -dependent activation of innate and adaptive immune responses or in TCR-dependent signaling pathways (Fig S10C).

Keeping the HECs transcriptional profile of NaCl-treated *Ifnar1*^{fl/fl} mice as a point of reference, a total of 566 genes were differentially expressed (DEGs) in HECs isolated from NaCl-treated VeCad^{*Ifnar1*-KO} mice, of which 373 (mostly ISGs and genes involved in the immune response or in the antigen processing) were downregulated (Fig 6A-C). These latter

results indirectly suggest that – when compared to HECs capable of sensing low levels of endogenous type I IFNs, as those present in NaCl-treated *Ifnar1^{fl/fl}* mice – LSECs devoted of *Ifnar1* may be less prepared to stimulate innate and adaptive immunity (Fig 6B). The downregulation of transcripts involved in cell-cell adhesion molecules and matrix remodeling (Fig S10D) further suggests a relative unpreparedness of VeCad^{*Ifnar1*-KO} HECs at accommodating changes that may confer protection against CRC trans-sinusoidal cell migration. Along these lines, the upregulation of the transcripts for *Gata4* -a master-regulator of liver sinusoidal differentiation which leads to liver fibrosis deposition upon its loss (Winkler et al, 2021)- and *Smad7* - an inhibitor of transforming growth factor-beta (TGF-β) dependent subendothelial matrix deposition causative of sinusoidal capillarization (Tauriello et al., 2018) - in HECs isolated from NaCl-treated VeCad^{*Ifnar1*-KO} mice (Fig 6A) could be interpreted as a diminished capacity to shape a vascular antimetastatic barrier. Finally, Gene Ontology (GO) analysis of HECs confirmed that *Ifnar1*-proficient, but not *Ifnar1*-deficient, HECs upregulate transcriptional pathways involved in the production of immunostimulatory cytokines and chemokines, the capacity to process and present antigens or the regulation of immune responses (Fig 6D). Altogether, the data support the hypothesis that, upon IFNα sensing, HECs and particularly LSECs not only acquire a transcriptional profile that can reinforce their barrier function, but they may also enhance HECs/LSECs immunostimulatory functions contributing to antitumor activity.

Continuous IFNα sensing improves immunostimulatory properties of HECs to provide long-term tumor protection

First, HECs/LSECs isolated from the liver of *Ifnar1^{fl/fl}* or VeCad^{*Ifnar1*-KO} mice 7 days after continuous NaCl or IFNα treatment were assessed for the relative surface protein expression of MHC-I, CD86 (a costimulatory molecule (Katz et al, 2004)) or the interleukin 6 receptor alpha (IL-6RA, a molecule that LSECs use to properly cross-prime antigens to

naïve CD8⁺ T cells (Bottcher *et al*, 2014)). Following IFN α treatment, *Ifnar1*-bearing LSECs significantly increased MHC-I, CD86 and IL-6RA expression (Fig S11A), while no induction was detected in *Ifnar1*-negative LSECs (Fig S11A). We then analyzed the ability of IFN α -treated LSECs or splenic DCs (sDCs) from *Ifnar1*^{fl/fl} and VeCad^{*Ifnar1*-KO} mice to stimulate the cross-priming of naïve CD8⁺ T cells *in vitro*. To this end, viable CD31⁺ HECs and CD11c⁺ sDCs were isolated and purified (Fig S12A,B). sDCs were cultured to acquire mature CD8 α ⁺ (~25%) or plasmacytoid (45%-50%) phenotypes endowed with cross-priming capacity (Fig S12C,D) (Fu *et al*, 2020). HECs and sDCs from *Ifnar1*^{fl/fl} or VeCad^{*Ifnar1*-KO} mice previously pulsed with the SIINFEKL peptide or soluble ovalbumin (sOVA) in the presence or absence of either IFN α or NaCl were then co-cultured with naïve OT-I CD8⁺ T cells and their relative cross-priming capacity was defined by the percentage of these latter cells to express both CD44 and IFN γ (Fig S11B). IFN α stimulation of *Ifnar1*-bearing HECs (HECs from *Ifnar1*^{fl/fl} mice or sDCs from *Ifnar1*^{fl/fl} and VeCad^{*Ifnar1*-KO} mice) pulsed with SIINFEKL or sOVA promptly increased their cross-priming capacities, while the same IFN α treatment failed to do so in *Ifnar1*-negative cells (HECs from VeCad^{*Ifnar1*-KO} mice) (Fig 7A,B and Fig S11B,C). Once exposed to IFN α and pulsed with sOVA, HECs and sDCs from *Ifnar1*^{fl/fl} mice cross-primed naïve OT-I CD8⁺T cells to a similar extent (Fig 7B and Fig S11C), highlighting once more the immunostimulating potential of IFN α treatment on HECs, including LSECs. We also evaluated the splenic composition of central memory T cell populations (Tcm, CD8⁺CD44⁺CD62L⁺) (Fig 7C and Fig S11D) as a proxy of potential systemic memory responses against tumor antigens (Sallusto *et al*, 2004; Stone *et al*, 2009; Yu *et al*, 2019). Splenic naïve T cells (Tn, CD8⁺CD44⁻CD62L⁺) were also evaluated. Looking at *Ifnar1*^{fl/fl} or VeCad^{*Ifnar1*-KO} mice continuously treated with NaCl or IFN α and euthanized by day 21 after challenge, we found that only IFN α -treated *Ifnar1*^{fl/fl} mice showed an increased proportion of Tcm and decreased percentage of Tn when compared to NaCl-treated *Ifnar1*^{fl/fl} controls (Fig

7C), suggesting that IFN α -responsive LSECs may promote antitumor immune memory in secondary lymphoid organs.

To assess whether IFN α -stimulated HECs and LSECs promoted memory responses endowed with antitumor potential, *Ifnar1^{fl/fl}*-cured mice (defined as animals that 7 days after IFN α treatment initiation were intrasenterically challenged with MC38 cells and survived as disease-free animals until day 50) or naïve *Ifnar1^{fl/fl}* control mice were subcutaneously rechallenged with MC38 cells (Fig 7D). Notably, while the latter animals developed subcutaneous tumors that increased in size over time, none of the *Ifnar1^{fl/fl}*-cured mice showed detectable lesions at any time point studied (Fig 7E). These results indicate that continuous IFN α treatment promotes protection against secondary tumor challenge even after IFN α therapy discontinuation. The results also suggest that this effect may be dependent on the capacity of IFN-sensitive HECs and LSECs to foster antitumor immunity, especially tumor-specific effector CD8⁺ T cell responses that are well-known to control tumor growth *in vivo* in different experimental settings (Dobrzanski *et al*, 2000; Katlinski *et al.*, 2017; Klebanoff *et al*, 2005; Yu *et al.*, 2019).

Discussion

In this study, we used different mouse models of CRC liver metastasis to show that the continuous perioperative administration of relatively low IFN α doses provides significant antitumor potential *in vivo* without provoking overt toxicity. Moreover, under the pharmacological conditions we defined (route, dosage, treatment duration, and chemical nature of the recombinant protein), we did not observe counter-regulatory mechanisms affecting IFN α efficacy (Katlinski *et al.*, 2017), or significant systemic side effects, as our strategy avoids the short tissue-oscillatory IFN α bursts that are often achieved after high and pulsed administrations, often associated with efficacy-limiting toxicities (Weber *et al.*, 2015). These results are consistent with previous preclinical work indicating that the

422 intrahepatic delivery of IFN α through a gene/cell therapy approach curbs CRC liver
423 metastases by acting primarily on unidentified non-hematopoietic stromal cell populations
424 (Catarinella *et al.*, 2016).

425 Given the pleotropic nature of IFN α , we demonstrated that the antimetastatic activity of IFN α
426 is neither based on the direct inhibition of primary intracecal tumor growth, favoring the
427 hypothesis that IFN α therapy does not modify the number of cells that spread from primary
428 tumors and seed into the liver - nor on the direct inhibition of metastatic cell growth within
429 the liver. These data is consistent with the high IFN α concentrations required to activate the
430 "tunable" direct antiproliferative functions of this cytokine, likely exceeding the levels
431 achieved in our system (Catarinella *et al.*, 2016; Schreiber, 2017). In addition, IFN α therapy
432 does not require indirect stimulation of hepatocytes, HSCs, DCs, KCs or LCMs to exert its
433 antimetastatic functions. Rather, the results pinpointed HECs/LSECs as key local and early
434 sensors of IFN α that ultimately limit CRC cell invasion into the liver.

435

436 Mechanistically, we showed that IFN α -stimulated LSECs inhibit the trans-sinusoidal
437 migration of circulating CRC cells normally occurring within 24 hours of their initial
438 intrahepatic landing. This effect is associated with phenotypic changes that IFN α -stimulated
439 LSECs acquire or induce in the liver microenvironment. Among these changes, we observed
440 a reduction in the overall LSEC porosity (i.e., sinusoidal fenestrae were reduced in number
441 and size), an enhancement in the subendothelial deposition of basal membrane components
442 (including collagen IV and laminin) and an upregulation of Lyve-1, a marker of hepatic
443 capillarization (Pandey *et al.*, 2020; Wohlfeil *et al.*, 2019). Along these lines, it is noteworthy
444 that in the "healthy" liver, functioning as a common site for CRC metastases, LSECs contain
445 numerous fenestrae of up to 200 nm in diameter and normally lack the typical basal
446 membrane that characterizes the microvasculature of most other tissues and organs
447 (Jacobs *et al.*, 2010). It is also interesting to note that IFN α -stimulated LSECs promote

microvascular alterations like those typifying pathological conditions (e.g., initial hepatic capillarization and liver fibrosis (Pandey *et al.*, 2020; Wohlfeil *et al.*, 2019)) associated with impaired immune cell extravasation and reduced immune surveillance (Guidotti *et al.*, 2015) and reduction of hepatic metastases from solid tumors including CRCs (Wohlfeil *et al.*, 2019). This fits with the evidence that CRC patients suffering from chronic viral liver fibrotic diseases characterized by hepatic endogenous type I interferon production display lower incidence of hepatic metastases (Augustin *et al.*, 2013; Baiocchi *et al.*, 2019; Li Destri *et al.*, 2013). The existence that fibrotic liver diseases not associated with reduced metastatic risk (Kondo *et al.*, 2016) suggests that changes in the vascular hepatic niche other than matrix deposition play additional roles in this process. Indeed, IFN α stimulated LSEC-governed changes hampering CRC extravasation including the modification of the sinusoidal GCX that, by increasing its thickness and modifying its chemical composition, recapitulated conditions known to negatively regulate the trans-endothelial migration of tumor cells in other settings (Glinskii *et al.*, 2005; Mitchell & King, 2014; Offeddu *et al.*, 2021; Wilkinson *et al.*, 2020). The continuous administration of therapeutic low-doses of IFN α thus stimulate HECs/LSECs to shape a vascular antimetastatic barrier preventing the interaction between tumor cells and endothelial cells that are known to promote the extravasation of the former cells (Glinskii *et al.*, 2005; Mitchell & King, 2014; Wilkinson *et al.*, 2020). Accordingly, the enhanced expression of “pro-migratory” adhesion molecules and integrins that we observed in the liver of animals bearing IFN α -responsive LSECs appear to be efficiently counteracted by the creation of such vascular barrier.

The notion that IFN α treatment failed to shape the vascular antimetastatic barrier in mice carrying the *Ifnar1*-deficiency only in endothelial cells further strengthens this hypothesis and places HECs/LSECs at a center of a relevant antitumor process ultimately limiting CRC liver invasion. This concept is also indirectly supported by the fact that the increased

expression *Gata4* -a master-regulator of liver sinusoidal differentiation which leads to liver fibrosis deposition upon its loss (Winkler *et al.*, 2021)- and *Smad7* - an inhibitor of transforming growth factor-beta (TGF- β) dependent subendothelial matrix deposition and sinusoidal capillarization (Tauriello *et al.*, 2018) were not downregulated by IFN α treatment in mice in which all cell types except LSECs could sense this cytokine, thus loosening the hepatic vascular barrier.

In addition, to hindering the initial trans-sinusoidal migration of CRC cells *in vivo*, IFN α -stimulated LSECs efficiently cross-presented nominal tumor antigens to naïve CD8⁺ T cells *in vitro*, enabling degrees of T cell priming and effector differentiation that were comparable to those induced by professional APCs. In keeping with this, we demonstrated that the *in vivo* IFN α stimulation of LSECs resulted in the upregulation of proteins and transcripts associated with antigen processing and presentation or co-stimulation (e.g. MHC-I, CD86, IL-6RA, *B2m*, *Tap1*, *Psmc-8/9* and *H2-d1*, *H2-k1/2*) (Bottcher *et al.*, 2014; Katz *et al.*, 2004; Montoya *et al.*, 2002; Rodriguez *et al.*, 1999). Moreover, our results also suggest that IFN α -stimulated LSECs may play a key role in antitumor immunity, as mice were protected from secondary tumor rechallenge even after discontinuation of IFN α treatment. The fact that the same IFN α therapy also significantly increased the overall number of central memory T cells in the spleen while decreasing that of naïve T cells (Sallusto *et al.*, 2004; Yu *et al.*, 2019) further suggests a role for IFN α -stimulated LSECs in the generation of systemic and protective long-term antitumor immunity.

These data are consistent with the notion that IFN α -stimulated LSECs, due to their anatomical proximity and efficient endocytosis capacity that is among the highest of all cell types in the body (Sorensen, 2020) - rapidly remove CRC-derived antigens from the intravascular space and productively and rapidly contribute to the development of effective

antitumor immunity, since this process does not require the time-consuming step of migration to lymphatic tissue (Bottcher *et al.*, 2014). This concept is also supported by the upregulation by IFN α -stimulated LSECs of *Cxcl9* and *Cxcl10*, two chemokines involved in the attraction and retention of naïve T cell populations of lymphocytes into the liver (Franciszkiewicz *et al.*, 2012), a necessary step for the generation of an efficient antitumor immune response. Additionally, other cell types within the hepatic niche could further amplify this IFN α -initiated cascade, as it has been shown that dendritic cells releasing IFN α also reduce liver metastatic colonization by CRC cells (Toyoshima *et al.*, 2019) and that this cytokine properly polarizes the tumor microenvironment (Catarinella *et al.*, 2016; De Palma *et al.*, 2008). On the contrary, the notion that a minority of IFN α -treated animals develop small intrahepatic lesions that display similar proliferation, neoangiogenic and immunologic markers than untreated lesions highlights the possibility that CRC tumors, once established as macroscopic metastases, may become refractory and resistant to IFN α therapy by downregulating *Ifnar1* (Boukhaled *et al.*, 2021; Katlinski *et al.*, 2017). This would be consistent with the lack of efficacy of our approach in established orthotopic tumors within the cecal wall.

Altogether, we have identified a novel MoA by which IFN α functions as antitumor drug against CRC liver metastases. Whether the adoption of similar LSEC-stimulating IFN α treatments may also curb the hepatic growth of metastatic cells originating from other solid tumors, or if continuous IFN α treatment promote the generation of vascular barriers in other metastasis-prone organs remains to be determined (Crist & Ghajar, 2021). Based on the findings of this report we propose the following model: CRC cells emerging from the primary tumor reach the hepatic sinusoids via the portal circulation and arrest - mostly because of size constraints - at the portal side of the sinusoidal circulation. CRC cells then trans-sinusoidally migrate into the liver parenchyma and develop micrometastases that will

eventually grow overtime, promoting the generation of an immunosuppressive microenvironment. Continuous therapy with well-tolerated doses of recombinant IFN α , stimulates HECs/LSECs to limit CRC trans-sinusoidal migration and parenchymal invasion by building up a vascular barrier typified by the reduction of LSECs porosity, the increased thickness of GCX and the appearance of a basal membrane. Continuous IFN α therapy also promotes long-term antitumor immunity in cured mice and protection from secondary tumor challenge, by stimulating LSECs to efficiently cross-prime tumor antigens to naïve CD8⁺ T cells (Fig 7F).

In terms of future clinical applications, our strategy could be used as perioperative neoadjuvant immunotherapy in CRC patients undergoing resection of their primary tumor who are at high risk for developing metachronous liver metastases (Engstrand *et al*, 2019; van Gestel *et al*, 2014). Indeed, several technologies have already been developed for the sustained release of drugs, such as osmotic pumps, electronic devices, hyaluronic acid-based hydrogels (Park *et al*, 2018; Stewart *et al*, 2018; Yun & Huang, 2016), FDA-approved polymer miscellas - such as pegylated (PEG)-IFN α (Foser *et al*, 2003; Glue *et al*, 2000) - and IFN α cell/gene therapy approaches (Catarinella *et al.*, 2016), which could quickly translate our results into clinical practice. Of note, the use of clinically approved doses of pegylated-IFN α has shown improved serum stability and clinical efficacy and reduced side effects, with serum IFN α concentrations similar to those achieved in our system (Foser *et al*, 2003; Glue *et al.*, 2000).

All in all, the results of this study support the use of continuous low doses of IFN α as an antimetastatic drug during the perioperative period, due to its ability to transform a metastases-prone liver into a metastases-resistant organ.

552 Materials and Methods

553 Reagents and Tools table

Reagent/Resource	Reference or Source	Identifier or Catalog Number
Experimental models: Organisms/strains		
Mouse: C57BL/6J	Charles River Lab	Strain code: 632
Mouse: BALB/c	Charles River Lab	Strain code: 028
Mouse: NSG	Charles River Lab	Strain code: 614
Mouse: B6(Cg)-Ifnar1 ^{tm1.1Ees/J} (Ifnar1 ^{fl/fl})	Jackson Lab	Stock No: 028256
Mouse: B6.Cg-Gt(ROSA)26Sor ^{tm6(CAG-ZsGreen1)Hze/J}	Jackson Lab	Stock No: 007906
Mouse: C57BL/6-Tg(Cdh5-cre/ERT2)1Rha (VeCad)	Taconic Biosci	Stock No: 13073
Mouse: B6.Cg-Tg(PDGFRβ-cre/ERT2)6096Rha/J (PDGFRβ)	Jackson Lab	Stock No: 029684
Mouse: B6.Cg-Speer6-ps1 ^{Tg(Alb-cre)21Mgn/J} (Alb)	Jackson Lab	Stock No: 003574
Mouse: B6.Cg-Tg(Itgax-cre)1-1Reiz/J (CD11c)	Jackson Lab	Stock No: 008068
Mouse: C57BL/6-Tg(TcraTcrb)1100Mgb/Crl (OT-I)	Jackson Lab	Stock No:003831
Antibodies		
anti-CD126, IL-6RA, conjugated to PE (clone D7715A7)	Biolegend	Cat# 115806, RRID:AB_313676
anti-CD18, ITGB2, conjugated to AF488 (clone M18/2)	Biolegend	Cat# 101402, RRID:AB_312811
anti-CD49d, ITGA4, conjugated to PE (clone 9C10(MFR4.B))	Biolegend	Cat# 103706, RRID:AB_313046
anti-H-2K ^b /H-2D ^b conjugated to FITC (clone 28-8-6)	Biolegend	Cat# 114605, RRID:AB_313596
anti-CD86 conjugated to PE (clone GL-1)	Biolegend	Cat# 105007, RRID:AB_313150
anti-CD146 conjugated to PE (clone ME-9F1)	Biolegend	Cat# 134704, RRID:AB_2143527
anti-CD44 conjugated to BV510 (clone IM7)	Biolegend	Cat# 103044, RRID:AB_2650923
anti-CD62L conjugated to AF488 (clone MEL-14)	Biolegend	Cat# 104420, RRID:AB_493376
Anti-IFNAR1 conjugated to PE (clone MAR1-5A3)	Biolegend	Cat# 127312 RRID:AB_2248800
InVivo MAb anti-mouse CD16/CD32, dilution 1:100	BioXCell	Cat# BE0307; RRID:AB_2736987
Antibodies for Immunofluorescence		
anti-GFP, dilution 1:100	Thermo Fisher Sci	Cat# A11122, RRID:AB_221569
Anti-GFP conjugated to AF488 (clone FM264G), dilution 1:100	Biolegend	Cat# 338008, RRID:AB_2563288
anti-CD31, PECAM1, dilution 1:300	R&D Systems	Cat# AF3628
anti-PDGFRβ, CD140b (clone APB5), dilution 1:200	eBioscience	Cat# 14-1402-82, RRID:AB_467493
anti-CD11c, (clone N418), dilution 1:100	Biolegend	Cat#117312, RRID:AB_492850
anti-Heparan Sulfate (clone F58-10E4), dilution 1:50	Amsbio	Cat# 370255-S
anti-LYVE-1, dilution 1:300	Novus Biol	Cat# NB600-1008
anti-Collagen type IV, dilution 1:100	Abcam	Cat# ab19808
anti-Laminin, dilution 1:300	Sigma-Aldrich	Cat# L9393
anti-CD54, ICAM1 (clone YN1/1.7.4), dilution 1:100	Biolegend	Cat#116101, RRID:AB_313692
anti-CD62E, E-selectin (clone 10E9.6), dilution 1:100	BD Bioscience	Cat#550290, RRID:AB_393585
donkey anti-Rabbit AF488, dilution 1:200	Thermo Fisher Sci	Cat#32790, RRID:AB_2762833
donkey anti-Goat AF546, dilution 1:200	Thermo Fisher Sci	Cat#A-11056, RRID:AB_2534103
donkey anti-Rat AF647, dilution 1:200	Jackson IR	Cat#712-605-153,RRID:AB_2340694
anti-IgM conjugated to APC (clone II/41), dilution 1:100	Thermo Fisher Sci	Cat#17-5790-82, RRID:AB_469458
Antibodies for Immunohistochemistry		
anti-Ki-67 (clone SP6) dilution 1:200	Thermo Fisher Sci	Cat# MA5-14520, RID:AB_10979488
anti-CD34 (clone MEC14.7) dilution 1:300	Biolegend	Cat# 119301, RRID:AB_345279
anti-F4/80 (clone A3-1) dilution 1:200	Bio-Rad	Cat# MCA497, RRID:AB_2098196

anti-CD3 (clone SP7) dilution 1:100	Abcam	Cat# ab21703, RRID:AB_446487
Anti-pSTAT1 (Clone 58D6) dilution 1:800	Cell Signaling	Cat# BK9167S, RRID: AB_561284
Antibodies for MACS		
anti-CD11c microbeads ultrapure	Miltenyi Biotec	Cat# 130-125-835
anti-F4/80 microbeads ultrapure	Miltenyi Biotec	Cat# 130-110-443
Chemicals, Enzymes and other reagents		
Recombinant mouse IFN α , carrier-free	Biolegend	Cat# 751802
Gadoxetic acid (Gd-EOB-DTPA); Primovist	Bayer S.p.A.	N/A
Tamoxifen	Sigma Aldrich	Cat# T5648-5G
Lipofectamine 2000	Thermo Fisher Sci	Cat# 11668019
NH ₂ -SIINFEKL-COOH (SL-8 peptide)	Proimmune	Cat# GMPT5995
Albumin from chicken egg white (ovalbumin)	Sigma-Aldrich	Cat# 55039
Paraformaldehyde powder	Sigma-Aldrich	Cat# 158127
Sodium Cacodylate powder	Sigma-Aldrich	Cat# C0250
25% EM grade Glutaraldehyde	ProSciTech	Cat# C001
Osmium tetroxide	ProSciTech	Cat# C011
Lanthanum (III) nitrate hexahydrate	MERK	Cat# 331937-11G
Zinc formalin fixative	Sigma-Aldrich	Cat# Z2902-3.75L
Fibronectin human plasma	MERK	Cat# F2006-1MG
Percoll®	Sigma-Aldrich	Cat# P4937-500ML
Alzet osmotic pumps 1002	Alzet	Cat# 10104844
Alzet osmotic pumps 1004	Alzet	Cat# 10104846
Matrigel Matrix	BD Bioscience	Cat# 354248
7-AAD Viability staining solution	Biolegend	Cat# 420404
InVivoMab anti-mouse GM-CSF (clone MP1-22E9)	BioXcell	Cat# BE0259
EGM™-2MV endothelial cell growth medium-2 BulletKit™	Lonza	Cat# CC-3202
Brefeldin A	Sigma-Aldrich	Cat# B7651
Commercial assays		
VeriKine-HS Mouse IFN α All-Subtype ELISA Kit	PBL Assay Sci	Cat# 42115-1
GeneArt™ CRISPR Nuclease Vector with OFP Reporter Kit	Thermo Fisher Sci	Cat# A21174
TOPO™ TA Cloning™ Kit	Thermo Fisher Sci	Cat# 450641
CellTiter-Glo® Luminescent Cell Viability Assay	Promega	Cat# G7570
ReliaPrep™ RNA Cell Miniprep System	Promega	Cat# Z6011
ReliaPrep™ RNA Tissue Miniprep System	Promega	Cat# Z6111
TURBO DNA-free™ kit	Ambion	Cat# AM1907
QIAamp DNA Mini kit	Qiagen	Cat# 51304
RNeasy Mini Kit	Qiagen	Cat# 74104
Procyte kit	Idexx	Cat# 9926306-00
Live/Dead fixable near-IR dead cell stain kit, dilution 1:500	Thermo Fisher Sci	Cat# L34975
Live/Dead fixable Green dead cell stain kit, dilution 1:100	Thermo Fisher Sci	Cat# L34970
DNAse TURBO	Thermo Fisher Sci	Cat# AM1907
Foxp3/Transcription Factor Staining buffer set	Thermo Fisher Sci	Cat# 00-5523-00
Experimental models: Cell lines		
CT26	ATCC	Cat# CRL-2638, RID:CVCL_7256
MC38	(Rosenberg <i>et al.</i> , 1986)	RRID:CVCL_B288
CT26 ^{LM3}	This paper	N/A
MC38-GFP	(Talamini <i>et al.</i> , 2021)	N/A
MC38 ^{IFNAR1_KO}	This paper	N/A
Oligonucleotides		
ACTCAGGTTTCGCTCCATCAG	(Prigge <i>et al.</i> , 2015)	Ifnar1 intron 3 forward
GCACATTGACCATTACAAGAGTAG	(Prigge <i>et al.</i> , 2015)	Ifnar1 intron 3 reverse
TCCAAGACTCCTGCTGTC	This paper	Ifnar1 exon2 forward
GCACTTTTACTTGCTCGGT	This paper	Ifnar1 exon2 reverse
ACTTGGCAGCTGTCTCCAAG	Jackson Lab	CD11c-Cre forward
GTGGCAGATGGCGCGGCA	Jackson Lab	CD11c-Cre reverse
CCAGGCTAAGTGCCCTTCTCTACA	Jackson Lab	ALB-Cre forward
AATGCTTCTGTCCGTTTGCCGGT	Jackson Lab	ALB-Cre reverse

GAAGTGTACACCGGGAGGA	Jackson Lab	PDGFRb-Cre forward
AGGCAAATTTTGGTGTACGG	Jackson Lab	PDGFRb-Cre reverse
GCCTGCATTACCGGTCGATGCAACG	This paper	VeCad-Cre forward
GTGGCAGATGGCGCGGCAACACCAT	This paper	VeCad-Cre reverse
AACCAGAAGTGGCACCTGAC	Jackson Lab	RosaZsgreen mutant forward
GGCATTAAAGCAGCGTATCC	Jackson Lab	RosaZsgreen mutant reverse
TAGACGTCTATATTCTCAGGGTTTT	This paper	crRNA1
ATGTAGACGTCTATATTCTCGTTTT	This paper	crRNA2
Mm00516793_g1	Applied Biosystem	Taqman probe Irf7
Mm00836412_m1	Applied Biosystem	Taqman probe Oas1
Mm 99999915_g1	Applied Biosystem	Taqman probe GAPDH
Instruments		
ProCyt Dx Hematology Analyzer	IDEXX Lab	N/A
Bruker Horizontal 7-Tesla MRI scanner	BioSpec	N/A
ViiA7 Fast Real-Time PCR System	Applied Biosys	Cat# 4453543
Aperio Scanscope XT Leica	Leica Biosystems	RRID:SCR_018457
Leica SP8 LIGHTNING confocal microscope	Leica Biosystems	RRID:SCR_018169
FEI Talos L120C G2 Transmission electron microscope	Thermo Fisher Sci	N/A
Zeiss FEG Gemini 500 Scanning electron microscope	Zeiss	N/A
FACSCanto™ II High Throughput Sampler	BD Bioscience	N/A
FACS LSRFortessa	BD Bioscience	N/A
FACSAria™ Fusion	BD Bioscience	N/A
Illumina NovaSeq 6000 machine	Illumina	RRID:SCR_016387
Agilent TapeStation 4100	Agilent	N/A
Leica CM1520 Cryostat	Leica Biosystems	RRID:SCR_017543
Labsystems Multiskan Ascent (Model 354)	Thermo Fisher Sci	N/A
Leica VT1000S Vibratome	Leica Biosystems	RRID:SCR_016495
Q150T ES Plus – Turbomolecular pumped coater	Quorum Tech	N/A
EM UC7 ultramicrotome	Leica Biosystems	RRID:SCR_016694
Software and algorithms		
FlowJo v10.5 or greater	Tree Star	RRID:SCR_008520
Prism version 8 or greater	GraphPad	RRID:SCR_002798
ImageScope software	Leica Biosystems	RRID:SCR_014311
Imaris version 7.2.3	Bitplane	RRID:SCR_007370;
Fiji software or ImageJ software	NIH	RRID:SCR_002285;003070
MIPAV v5.3.4 or greater	CIT, NIH	RRID:SCR_007371
EsivisionPro 3.2 software	Soft Imaging Sys	N/A
OsiriX DICOM viewer version 3.9.2 or greater	Pixmeo SARL	N/A
Trimmomatic version 0.32	(Bolger <i>et al</i> , 2014)	RRID:SCR_011848
STAR aligner version 2.5.3a	STAR SRL	RRID:SCR_004463
GENECODE version M22	Ensembl 97	N/A
R-4.0.3 software	R Core Team	N/A
DESeq2 version 1.30.1	(Love <i>et al</i> , 2014)	N/A
EnrichR R package version 3.3	(Chen <i>et al</i> , 2013)	RRID:SCR_020938
GeneArt™ CRISPR Search and Design Tool	Thermo Fisher Sci	N/A
BioRender	BioRender	RRID:SCR_018361
Deposited data		
Intrahepatic CD31 bulk RNA-seq	GEO database	GSE186203

Methods and Protocols

Animal studies. Eight-to ten-week-old C57BL/6J and BALB/c mice were purchased from Charles River Laboratory, Calco, Italy. CB6 mice were obtained by crossing *M. m. domesticus* inbred C57BL/6 male mice (H-2b restricted) with *M. m. domesticus* inbred BALB/c female mice (H-2d restricted), to produce H-2bxd F1 hybrids. *Ifnar1^{fl/fl}* mice on a

560 C57BL/6J background (B6(Cg)-*Ifnar1*^{tm1.1Ees/J}), PDGFR β ^{CreERT2} (B6.Cg-Tg(PDGFR β -
561 cre/ERT2)6096Rha/J), Alb^{Cre} (B6.Cg-Speer6-ps1Tg(Alb-cre)21Mgn/J), CD11c^{Cre} (B6.Cg-
562 Tg(Itgax-cre)1-1Reiz/J), and Rosa26-ZsGreen (B6.Cg-Gt(ROSA)26Sortm6(CAG-
563 ZsGreen1)Hze/J) reporter mice were purchased from the Jackson Laboratory. Cdh5(PAC)-
564 CreERT2 mice (VeCad^{CreERT2})(Wang *et al.*, 2010) were kindly provided by S. Brunelli
565 (UniMib, Milan). NOD-scid IL2R γ null (NSG) immunodeficient mice (C57BL/6-
566 Tg(TcraTcrb)1100Mgb/Crl) and C57BL/6-Tg(TcraTcrb)1100Mgb/Crl (OT-I) mice were
567 purchased from Charles River Laboratory. All animal experiments were approved by the
568 Animal Care and Use Committee of the San Raffaele Scientific Institute (IACUC 691, 808
569 and 1042) and were conducted in specific pathogen-free (SPF) facility in microisolator cages
570 under a 12-hour light/dark cycle with free access to water and standard mouse diet (Teklad
571 Global 18% Protein Rodent Diet, Harlan).

572 The conditional deletion of *Ifnar1* was obtained by crossing mice carrying loxP-flanked
573 *Ifnar1*(Prigge *et al.*, 2015) with transgenic mice expressing Cre recombinase under the
574 control of either endothelial cell (VeCad^{CreERT2}), stellate cell (PDGFR β ^{CreERT2}), hepatocyte
575 (Alb^{Cre}) and dendritic cell (CD11c^{Cre}) promoters. To induce the Cre recombination and *Ifnar1*
576 deletion into VeCad^{CreERT2}, Cre recombinase was induced by three subcutaneous injections
577 of Tamoxifen 50mg/kg at p5, p6 and p7, as previously described(Tirone *et al.*, 2018), while
578 PDGFR β ^{CreERT2} adult mice were treated by three consecutive ip injections of Tamoxifen
579 100mg/kg. Upon treatment, the exon3 of *Ifnar1* is excised resulting in a loss of *Ifnar1* in
580 endothelial and stellate cells. To ensure that *Ifnar1* exon 3 of was efficiently excised hepatic
581 DNA was isolated from the liver of 8-week-old VeCad^{*Ifnar1*_KO}, PDGFR β ^{*Ifnar1*_KO}, Alb^{*Ifnar1*_KO}
582 and CD11c^{*Ifnar1*_KO} mice and polymerase chain reaction (PCR) analysis using *Ifnar1* intron
583 3-forward and *Ifnar1* intron 3-reverse oligonucleotides was performed. To control for
584 possible changes in the microbiota composition of VeCad^{*Ifnar1*_KO}, PDGFR β ^{*Ifnar1*_KO},
585 Alb^{*Ifnar1*_KO} and CD11c^{*Ifnar1*_KO} and *Ifnar1*^{fl/fl} littermates, mice from each litter and cage were

randomly allocated into the experimental groups and were co-housed or systematically exposed to beddings of the other groups to ensure the same exposure to the microbiota.

CRC cell lines. CT26 (H-2d, BALB/c-derived) cell line was purchased from ATCC. MC38 (H-2b, C57BL/6-derived), have been previously described (Catarinella *et al.*, 2016). MC38 cells were transduced with a PGK-GFP lentiviral vector, cloned and sorted by FACS to establish MC38^{GFP} fluorescently tagged cell lines (Talamini *et al.*, 2021). All cells were routinely tested for mycoplasma contamination using the N-GARDE Mycoplasma PCR reagent set (EuroClone). CT26 and CT26^{LM3} cells were cultured under standard condition at 37°C in a humid atmosphere with 5% CO₂ in RPMI GlutaMAX medium (Gibco) supplemented with 10% FBS (Lonza) and 1% penicillin/streptomycin (P/S) (Gibco). MC38, MC38^{GFP}, MC38^{Ifnar1-KO} and cells were cultured under standard condition at 37°C in a humid atmosphere with 5% CO₂ in DMEM GlutaMAX medium (Gibco) supplemented with 10% FBS (Lonza) and 1% P/S (Gibco). Cell number and dimension was routinely assessed by automated CytoSMART cell counter (Corning).

Mouse models of liver metastases. Eight-to ten-week-old sex- and age-matched mice were injected with 5x10³ CT26 or 5x10⁴ MC38 CRC cell lines either through intrasplenic or superior mesenteric vein injections as previously described (Catarinella *et al.*, 2016; van der Bij *et al.*, 2010). For early time point experiments, 7x10⁵ MC38^{GFP} cells were injected in the superior mesenteric vein of anesthetized mice as described (van der Bij *et al.*, 2010). For intrasplenic or superior mesenteric vein injections, deep anesthesia was induced by isoflurane inhalation (5% induction and 2% for maintenance in 2 l/min oxygen). The indicated number of CRC cells was injected into spleen or the superior mesenteric vein using a 29G needle and to prevent excessive bleeding vein puncture was compressed with a sterile and absorbable hemostatic gauze (TABOTAMP®). The peritoneum and skin were sutured with

silk 4.0 and 7 mm wound clips as described (Catarinella *et al.*, 2016). This experimental setting may mimic the vascular spreading of CRC cells during primary tumor resection and, thus, preventive IFN α infusion may be considered as a neoadjuvant treatment.

Mouse model of orthotopic colorectal cancer liver metastases. The generation of highly metastatic CT26 CRC cells was obtained by 3 consecutive rounds of *in vivo* selection as previously reported (Zhang *et al.*, 2013). Briefly, 2×10^6 CT26 cells were first injected subcutaneously into the right flank of immunodeficient NSG mice. After 28 days, tumors were excised, dissected, sliced into small fragments, and digested for 30 minutes at 37°C in DMEM containing collagenase type IV (200 units/ml; Sigma-Aldrich) and DNase I (100 units/ml; Sigma-Aldrich). The resulting cell suspension defined as CT26^{sc}, were maintained at 4°C, filtered through a 70 μ m nylon cell strainer (BD Biosciences, Bedford, MA), washed in PBS, and grown in RPMI 10% FBS. Sub-confluent CT26^{sc} cells were harvested, resuspended in PBS:Matrigel (1:1) (Corning, MERK) and then injected into the cecal wall of immune competent anesthetized (isoflurane, 5% induction and 2% for maintenance in 2 l/min oxygen), CB6 recipient mice as described (Zhang *et al.*, 2013). Briefly, a midline incision was made to exteriorize the cecum. Using a 33G micro-injector (Hamilton, USA), 10 μ l of a 50% Matrigel solution (BD Bioscience, USA) containing 2×10^5 CT26^{sc} cells were injected into the cecum wall. To avoid intraperitoneal spreading of CT26^{sc}, the injection site was sealed with tissue adhesive (3M Vetbond, USA) and washed with 70 % alcohol. The cecum was replaced in the peritoneal cavity, and the abdominal wall and skin incision was sutured with silk 4.0 and 7 mm wound clips as described (Catarinella *et al.*, 2016). Twenty-eight days after injection, mice were euthanized and single cell suspensions of liver metastatic lesions, defined as CT26^{LM1}, were obtained as described above. This cycle was repeated twice to obtain the highly metastatic CT26^{LM3} cells.

Recombinant Mouse IFN α therapy. Continuous intraperitoneal IFN α delivery (IFN α 1 carrier-free, Biolegend, San Diego, CA, USA) was achieved by intraperitoneal implantation of mini-osmotic pumps (MOP, ALZET, Cupertino, CA, USA) able to deliver either 50, 150 or 1050 ng IFN α a day for 14 or 28 days. NaCl-containing MOP were used as controls. MOP filling, priming and implantation within the peritoneum was performed following manufacturer's instructions. To avoid MRI artifacts due to the presence of metallic components within MOP, the day before MRI acquisition, MOP were removed from the peritoneum. To directly investigate responsiveness of liver cells to IFN α , signaling downstream of *Ifnar1* receptor was assessed by measuring pSTAT1 by IHC 30 minutes after an ip injection of NaCl or 1 μ g IFN α , a dose able to synchronize pSTAT1 expression in all *Ifnar1* expressing cells (Lin *et al*, 2016).

Tumor rechallenge of IFN α cured mice. IFN α -cured mice that were designated as MC38-tumor free for at least 50 days after challenge, were subcutaneously rechallenged with 5x10³ MC38 cells resuspended in 200 μ l of PBS:Matrigel (1:1). Age-matched naïve syngeneic mice were used as control. Tumor volumes were measured twice a week and euthanized for ethical reasons when tumor size reached ~ 500 mm³.

Magnetic resonance imaging (MRI). All MRI studies were carried out at the Experimental Imaging Center of SRSI on a preclinical 7-Tesla MR scanner (Bruker, BioSpec 70/30 USR, Paravision 6.0.1, Germany) equipped with 450/675 mT/m gradients (slew rate: 3400/4500 T/m/s; rise time 140 μ s), coupled with a dedicated 4 channels volumetric mouse body coil. All images were acquired in vivo, under inhalational anesthesia (Isoflurane, 3% for induction and 2% for maintenance in 1L/minute oxygen) with mice laid prone on the imaging table. A dedicated temperature control system was used to prevent hypothermia; respiratory rate and body temperature were continuously monitored (SA Instruments, Inc., Stony Brook, NY,

664 USA) during the whole MRI scan. An intravenous injection of gadoxetic acid (Gd-EOB-
665 DTPA; Primovist, Bayer Schering Pharma) at a dose of 0.05 $\mu\text{mol/g}$ of body weight was
666 administered via the tail vein before placing the mice on the scanner table. As previously
667 described (Sitia *et al*, 2012), the MRI studies relied on an axial fat-saturated T2-weighted
668 sequence (TurboRARE-T2: TR=3394ms, TE=33ms, voxel-size=0.125x0.09x0.8mm,
669 averages=3) acquired immediately after Gd-EOB-DTPA injection and an axial fat-saturated
670 T1-weighted scan (RARE-T1: TR=581ms, TE=8.6ms, voxel-size=0.125x0.07x0.8mm,
671 averages=4) acquired thereafter, during the hepatobiliary phase (HBP) of contrast excretion
672 (starting from 10 minutes after Gd-EOB-DTPA injection). Two board certified radiologists
673 skilled in clinical and preclinical abdominal MR imaging, blinded to any other information,
674 reviewed all MRI studies using an open-source image visualization and quantification
675 software (Mipav, 5.3.4 and later versions, Biomedical Imaging Research Services Section,
676 ISL, CIT, National Institute of Health, USA). Liver metastases were identified as focal lesions
677 showing slight hyper-intensity on T2-weighted images and concurrent hypo-intensity on
678 contrast-enhanced HBP T1-weighted images. Liver metastases segmentation was
679 performed by manual drawing of regions-of-interest (ROIs) on each slice, yielding volumes-
680 of-interest (VOIs; lesion area x slice thickness) for the entire sequence. The total CRC
681 metastatic mass was obtained by summing up the volumes of all single VOIs that were semi-
682 automatically provided by the software.

683

684 **MC38 gene editing.** To knockout *Ifnar1* in MC38 cell line, we used GeneArt™ CRISPR
685 Nuclease Vector with OFP Reporter Kit (ThermoFisher Scientific). Target-specific CRISPR
686 RNA guides (crRNA) were designed using GeneArt™ CRISPR Search and Design Tool
687 (ThermoFisher Scientific) and the two following crRNAs with the fewest predicted off-target
688 effects were selected: crRNA1: TAGACGTCTATATTCTCAGGGTTTT; crRNA2:
689 ATGTAGACGTCTATATTCTCGTTTT. Annealed crRNAs were cloned in GeneArt™

CRISPR Nuclease Vector with OFP according to the manufacturer's instructions and vector constructs were used to transform OneShot TOP10 chemically competent E. Coli cells (ThermoFisher Scientific). Vectors were validated by Sanger sequencing of DNA from 10 colonies for each crRNA (LightRun GATC Carlo Erba). To express the CRISPR-Cas9 system transiently, 2 µg of each vector were used to transfect 5x10⁵ MC38 cell line with Lipofectamine 2000 (ThermoFisher Scientific) in Opti-MEM medium (ThermoFisher Scientific). After three days, transfection efficiency was evaluated measuring the orange fluorescence protein (OFP) by FACS (LSRFortessa) and data analysed using FlowJo v10.5. OFP positive bulk populations were single-cell cloned in 96-well plates and a total of 12 clones screened for mismatches by T7E1 assay (New England Biolabs). Briefly, genomic DNA from MC38 clones was extracted by Qiaamp mini kit (Qiagen) and amplified within the exon 2 of *Ifnar1* locus using the following oligos: *Ifnar1* exon2 forward, TCCAAGACTCCTGCTGTC and *Ifnar1* exon2 reverse: GCACTTTTACTTGCTCGGT. The PCR products were denatured and annealed according to manufacture protocol (New England Biolabs). The digestion reaction was run onto 2% agarose gel to identify mismatched clones. Genetic validation of T7E1 positive clones was assessed by cloning the PCR products with TOPO™ TA Cloning™, Dual Promoter, Kit (ThermoFisher Scientific) and subsequently 10 clones per cell line were sequenced (LightRun GATC Carlo Erba). Functional validation of *Ifnar1* knockout MC38 cells was determined by RT-PCR for the ISG *Irf7* after 4 hours of *in vitro* stimulation with 300 ng/ml IFNα, using MC38 transfected non-edited WT clone as control (MC38).

Peripheral blood analyses. At the indicated time points after IFNα administration, whole anti-coagulated blood of MOP-NaCl and MOP-IFNα-treated mice was collected from the retro-orbital plexus of anesthetized animals (isoflurane, 5% for induction and 2% for maintenance in 2l/minute oxygen) using Na-heparin coated capillaries (Hirschmann

Laborgeräte GmbH, Germany) and vials (Microvette, Sarstedt, Germany). Hematologic parameters were evaluated using an automated cell counter (ProCyt Dx, IDEXX Laboratories, USA). The extent of hepatocellular injury was monitored by measuring serum ALT (sALT) activity at several time points after IFN α treatment, as previously described (Sitia *et al.*, 2012).

Measurement of plasma IFN α by ELISA. Circulating levels of IFN α were quantified in plasma collected from NaCl controls or IFN α -treated mice at indicated time points using VeriKine-HS Mouse IFN α all Subtype ELISA Kit (PBL) according to the manufacturer's instructions. The IFN α titer in the samples was determined by plotting the optical density (OD) subtracted of blank OD to eliminate background, using a 4-parameter logistic fit for the standard curve by using Prism v8 (GraphPad). Detection range is comprised between 2.38 and 152 pg/ml of IFN α .

RNA extraction and quantitative real-time PCR gene expression analyses. Total RNA was isolated from liver homogenates of MOP-NaCl control and MOP-IFN α -treated mice by using the ReliaPrepTM RNA Tissue Miniprep System (Promega) and DNase TURBO (Thermo Fisher Scientific) following manufacturer's recommendation. The extracted RNA was subsequently retro-transcribed to cDNA as previously described (Sitia *et al.*, 2011). Quantitative real-time PCR analysis was performed utilizing the ViiA7 Fast Real-Time PCR System (Applied Biosystems). The ISG, *Irf7* (Mm00516793_g1) as well as the housekeeping *Gapdh* (Mm 99999915_g1) were quantified by using the indicated FAM-MGB labeled TaqMan Gene Expression Assays (Applied Biosystems). Gene expression was determined as the difference between the threshold cycle (Ct) of the gene of interest (Goi) and the Ct of the housekeeping (*Gapdh*) of the same sample (Δ Ct). The fold-change expression of each Goi was calculated over its basal expression in the control sample by the formula $2^{-\Delta\Delta Ct}$ as

742 described (Sitia *et al.*, 2012).

743

744 **Immunohistochemistry.** At time of autopsy for each mouse, livers were perfused with PBS,
 745 harvested and different pieces were sampled, fixed in zinc-formalin, processed and
 746 embedded in paraffin for histological and immunohistochemical analysis, as previously
 747 described (Sitia *et al.*, 2012). Immunohistochemical staining using a Bond RX Automated
 748 Immunohistochemistry (Leica Microsystems GmbH, Wetzlar, Germany) was performed on
 749 3- μ m-thick sections. First, tissues were deparaffinized and pre-treated with the Epitope
 750 Retrieval Solution [ER1 Citrate Buffer for Ki-67 (dilution 1:200, clone SP6, Thermo Fisher
 751 Scientific) and F4/80 (dilution 1:200, clone A3-1, Bio-Rad); ER2 EDTA for CD3 (dilution
 752 1:100, clone SP7, Abcam), CD34 (dilution 1:300, clone MEC14.7, Biolegend) and pSTAT1
 753 (dilution 1:800, clone 58D6, Cell Signaling)] at 100°C for 30 min. After washing steps,
 754 peroxidase blocking was carried out for 10 min using the Bond Polymer Refine Detection Kit
 755 DS9800 (Leica Microsystems GmbH). Then, tissues were washed and incubated for 1h RT
 756 with the primary antibody diluted in IHC Antibody Diluent (Novocastra, Leica RE7133).
 757 Subsequently, tissues were incubated with polymer-HRP or Rat-on-Mouse HRP (Biocare
 758 Medical, RT517H), developed with DAB-Chromogen for 10 min and counterstained with
 759 Hematoxylin for 5 min. For image acquisition and analysis eSlide Manager (Aperio Leica
 760 Biosystems) was used. All images were acquired using the Aperio AT2 system (Leica
 761 Biosystems). Quantifications were performed by automated image analysis software
 762 through dedicated macros of the ImageScope program, customized following
 763 manufacturer's instructions (Leica Biosystems). The images shown were identified as
 764 representative area of interest within the total area of the specimen analyzed and exported
 765 as ImageScope snapshots.

766

767 **Immunofluorescence and confocal microscopy.** Livers were perfused with PBS,

768 harvested and fixed over-night in 4% paraformaldehyde (PFA), equilibrated in 30% sucrose
 769 in PBS over-night at 4°C prior to embedding in OCT (Bio-Optica) for quick freezing at -80°C.
 770 30-µm-thick cryosections were adhered to Superfrost Plus slides (Thermo Scientific). For
 771 immunofluorescence staining, sections were blocked and permeabilized with PBS
 772 containing 5% FBS and 0.1% Triton X-100 (Sigma-Aldrich) for 30 min at room temperature
 773 and subsequently incubated with 10% of donkey serum (DS; Sigma-Aldrich) in PBS for 30-
 774 60 min at room temperature. Staining with primary and secondary antibodies, were
 775 performed with staining buffer (PBS with 1.5% DS, 0.2% Triton X-100 and 1% BSA), using
 776 the following antibodies and dilutions: anti-PDGFRβ/CD140b (dilution 1:200, clone APB5,
 777 eBioscience) + anti-rat AF647 (dilution 1:200, Jackson IR); anti-CD11c AF647, (dilution
 778 1:100, clone N418, Biolegend); anti-GFP (dilution 1:100, rabbit polyclonal, A11122 Thermo
 779 Fisher Scientific) + anti-rabbit AF 488 (dilution 1:200, Thermo Fisher Scientific); anti-
 780 CD31/PECAM-1 (dilution 1:300, goat polyclonal, AF3628 R&D Systems) + anti-goat AF546
 781 (dilution 1:200, Thermo Fisher Scientific); anti-Heparan Sulfate (dilution 1:50, clone F58-
 782 10E4, Amsbio) + anti-IgM conjugated to APC (dilution 100, clone II/41, Thermo Fisher
 783 Scientific); anti-LYVE-1 (dilution 1:300, rabbit polyclonal, Novus Biologicals) + anti-rabbit
 784 AF647 (dilution 1:200, Thermo Fisher Scientific); anti-Collagen type IV (dilution 1:100, rabbit
 785 polyclonal, Abcam) + anti-rabbit AF488 (dilution 1:200, Thermo Fisher Scientific); anti-
 786 Laminin (dilution 1:300, rabbit polyclonal, Sigma-Aldrich) + anti-rabbit AF488 (dilution 1:200,
 787 Thermo Fisher Scientific); anti-CD54/ICAM1 (dilution 1:100, clone YN1/1.7.4, Biolegend) +
 788 anti-rat AF647 (dilution 1:200, Jackson IR); anti-CD62E/E-selectin (dilution 1:100, clone
 789 10E9.6, BD Bioscience) + anti-rat AF647 (dilution 1:200, Jackson IR). Confocal images were
 790 acquired using a Leica SP8 confocal systems (Leica Microsystems) that are available at the
 791 SRSI Advanced Light and Electron Microscopy BioImaging Center (ALEMBIC). 15-20 µm z-
 792 stacks were projected in 2D and processed using Fiji image processing software (Schindelin
 793 *et al*, 2012). Localization of MC38^{GFP} tumor cells within liver vessels, 20-30 square xy

sections (1024 x 1024 pixel) confocal xyz stacks, from NaCl- and IFN α -treated mice, were acquired with 0.5 μ m z-spacing on a Leica TCS SP8. The Imaris Surpass View and Surface Creation Wizard were used to create 3D renderings of MC38^{GFP} cells and CD31⁺ liver vessels as previously reported (Guidotti *et al.*, 2015). A tumor cell was considered intravascular when at least 95% of its surface-reconstructed body was inside the vessel lumen in all the acquired sections projected in the horizontal (xy), transversal (yz) and longitudinal (xz) planes. Entire liver sections were acquired using MAVIG RS-G4 confocal microscope (MAVIG GmbH Research, Germany) to quantify the number of MC38^{GFP} tumor cells in relation to the total liver area. The quantification of the percentage of liver area covered by endothelial markers and extracellular matrix components, such as heparan sulfate, laminin, collagen type IV, ICAM1 and E-selectin, was evaluated using ImageJ software, applying the same threshold to the different experimental groups for each channel and measuring the percentage of area limited to threshold. Colocalization analysis of GFP in the different Cre recombinant mouse models was performed using an unsupervised ImageJ plugin algorithm termed Colocalization, which was developed by Pierre Bourdoncle (Institut Jacques Monod, Service Imagerie, Paris; 2003–2004).

Scanning and Transmission Electron Microscopy. Electron microscopy (EM) fixative composition was 2,5 % glutaraldehyde, 2% paraformaldehyde, 2 mM CaCl₂ and 2% sucrose in 0,1 M Na cacodylate buffer (pH 7,4). For the analysis of endothelial GCX the EM fixative was supplemented with 2% Lanthanum nitrate (MERK) as previously reported (Inagawa *et al.*, 2018). Warm PBS and EM fixative at 35-37°C was used to ensure tissue integrity. When mice were under deep anesthesia, with a single ip injection of 50-60 mg/kg Tribromoethanol (Avertin), a Y incision was made in the abdomen to expose the liver and the portal vein. The portal vein was cannulated with an appropriately sized IV cannula of 22G and the liver was perfused with 15 ml of warm PBS at a constant rate of 3 rpm using a peristaltic pump (Peri-

Star™ Pro, 2Biological Instruments) as previously reported (Guidotti *et al.*, 2015). *In situ* fixation was achieved by perfusing EM fixative for approximately 5 min at 3 rpm. Fixed liver was harvested and cut into 5 mm blocks using a scalpel. Liver blocks were ultimately immersed in EM fixative for 24-72 h at 4°C and finally EM fixative was replaced with 0.1 M sodium cacodylate buffer and stored at 4°C until processed for TEM or SEM analysis. Liver blocks were post-fixed in 1% osmium tetroxide (OsO₄), 1,5% potassium ferricyanide(K₄[Fe(CN)₆]) in 0,1M Na Cacodylate buffer for 1 h on ice. Afterwards, for SEM, 150 µm-thick sections were obtained from perfused livers using a vibratome (Leica VT1000S). Sections were further post-fixed in 1% OsO₄ in 0,1M Na Cacodylate, dehydrated through a series of increasing concentration of ethanol and immersed in absolute hexamethyldisilazane (HMDS) that was left to evaporate overnight. Dried sections were sputter-coated with Chromium using a Quorum Q150T ES sputter coater. Sections were then mounted on SEM stubs using conductive adhesive tape and observed in a field-emission scanning electron microscope Gemini 500, (ZEISS, Oberkochen, Germany). The LSEC fenestra measurements were performed from SEM microphotographs taken under a magnification of 20.000X, using 3 independent samples from each experimental condition [NaCl-*Ifnar1*^{fl/fl} (n=3), IFNα-*Ifnar1*^{fl/fl} (n=3), NaCl-VeCad^{*Ifnar1*^{-/-}} (n=3) and IFNα-VeCad^{*Ifnar1*^{-/-}} mice (n=3)] and a total area of about 720 µm² of sinusoids was analyzed for each mouse. After 40 days of IFNα discontinuation, 2 randomly selected liver micrographs of IFNα-*Ifnar1*^{fl/fl} (n=3) were analyzed to determine LSEC fenestra measurements and a total area of approximately 300 µm² of sinusoidal surface was analyzed. All measurements were made using the ImageJ software, as previously described (Cogger *et al.*, 2015). Briefly, the flattened area of the liver sinusoid was selected and longest diameter of each fenestrae was measured. Gaps larger than 250nm were excluded from the analysis. The average fenestration diameter (defined as the average of all fenestrae diameters excluding gaps area), the fenestration area (πr^2 , where r, the radius, was calculated from the individual

fenestrae diameter $r=d/2$, without gaps area), the porosity $[\Sigma(\pi r^2)/(\text{total area analyzed} - \Sigma(\text{area of gaps})) \times 100$; expressed as a percentage], and the fenestration frequency [total number of fenestrations/((total sinusoidal area analyzed - $\Sigma(\text{area of gaps})$); expressed as μm^2] have been calculated. Surface roughness analysis of endothelial GCX was determined using Image J software. The flattened area of the liver sinusoid was analyzed, with the SurfChartJ1Q plugin to determine the roughness deviation of all points from a plane after background subtraction, known as Ra coefficient as previously reported (Pavlovic *et al*, 2012). A representative area within the flatten liver sinusoidal surface was used to generate a 3D surface plot image.

For TEM, tissue pieces were rinsed in Na Cacodylate buffer, washed with distilled water (dH₂O) and enbloc stained with 0.5% uranyl acetate in dH₂O overnight at 4°C in the dark. Finally, samples were rinsed in dH₂O, dehydrated with increasing concentrations of ethanol, embedded in Epon resin and cured in an oven at 60°C for 48 h. Ultrathin sections (70 – 90 nm) were obtained using an ultramicrotome (UC7, Leica microsystem, Vienna, Austria), collected, stained with uranyl acetate and Sato's lead solutions, and observed in a Transmission Electron Microscope Talos L120C (FEI, Thermo Fisher Scientific) operating at 120kV. Images were acquired with a Ceta CCD camera (FEI, Thermo Fisher Scientific). TEM microphotographs were taken under a magnification of 3.400X, using 3 independent samples from each experimental condition and a total area of approximately 2.575 μm^2 was analyzed for each mouse. LSECs thickness and the width of the space of Disse were measured using ImageJ software. For collagen deposition analysis, at least 10 randomly selected sinusoids from each mouse were analyzed as previously reported (Gissen & Arias, 2015; Warren *et al*, 2007).

Isolation of liver non-parenchymal cells (NPCs). Liver NPCs, including leukocytes, were

isolated from NaCl control or IFN α -treated mice 7 days after MOP implantation, as previously described (Benechet *et al*, 2019). Briefly, after euthanasia, the liver was perfused through the vena cava with 5-8 ml of PBS to remove most blood cells. Livers were weighted and 50% of the tissue was sliced in small pieces and incubated 30 minutes at 37°C in 10 ml of digestion medium (RPMI GlutaMAX medium [Gibco] containing 200U/ml of collagenase type IV [Sigma-Aldrich] and 100 U/ml of DNase I [Sigma-Aldrich]). Remaining undigested fragments were syringed with an 18G needle and filtered through a 70 μ m cell strainer to obtain a single cell suspension. Cells were centrifuged 3 minutes at 50g at room temperature and the pellet containing hepatocytes was discarded. The resultant cell suspension of NPCs was incubated for 30 sec with ACK lysis buffer (Lonza) to deplete red blood cells, washed with cold RPMI. NPCs were counted and processed for flow cytometry analysis or sorting.

Isolation of splenocytes and naïve CD8⁺ T cells. Spleens were obtained from *Ifnar1^{fl/fl}* and *VeCad^{Ifnar1^{fl/fl}}* mice 21 days after MC38 cells challenge and placed in a 70 μ m cell strainer on a petri dish containing 10 ml of plain RPMI, ground with a syringe plunger to obtain a cell suspension and washed 3 times with plain RPMI as previously described (Sitia *et al.*, 2012). The cell suspension was centrifuged at 400g for 5 min at room temperature, the resuspended pellet was incubated for 30 sec with ACK lysis buffer and neutralized with RPMI. Resultant splenocytes were counted and processed for FACS analysis. Splenocytes derived from OT1 mice were prepared as described above and naïve CD8⁺ T cells were isolated using EasySep™ Mouse Naïve CD8⁺ T cell isolation kit (STEMCELL Technologies) following manufacturer's instructions.

Flow cytometry and cell sorting. Cells were resuspended in PBS and LIVE/DEAD™ Fixable Near-IR or Green dead cell dyes (Thermo Fisher Scientific) and incubated 15 min at RT in the dark for cell viability assessment. Subsequently, cells were blocked with FACS

898 buffer (PBS supplemented with 2% FBS) containing InVivo MAb anti-mouse CD16/CD32
899 (BioXCell) and stained for surface markers using the following antibodies: anti-CD45R/B220
900 (clone RA3-6B2, Biolegend), anti-CD11b (clone M1/70, Biolegend), anti-mouse CD11c
901 (clone N418, Biolegend), anti-CD3 (clone 145-2C11, Thermo Fisher Scientific), anti-CD45
902 (clone 30-F11, Biolegend), anti-CD8a (clone 53-6.7, Biolegend), anti-F4/80 (clone BM8,
903 Biolegend), anti-CD126/IL-6RA (clone D7715A7, Biolegend), anti-CD18/ITGB2 (clone
904 M18/2, Biolegend), anti-CD49d/ITGA4 (clone 9C10(MFR4.B), Biolegend), anti-H-2Kb/H-
905 2Db (clone 28-8-6, Biolegend), anti-CD86 (clone GL-1, Biolegend), anti-CD146 (clone ME-
906 9F1, Biolegend), anti-CD44 (clone IM7, Biolegend), anti-CD62L (clone MEL-14, Biolegend),
907 anti-IFN γ (clone XMG1.2, BD Biosciences), anti-CD31 (clone MEC13.3, BD Biosciences)for
908 20 min at 4°C. For intracellular IFN γ staining, cells were then fixed, permeabilized and
909 stained following Foxp3/Transcription Factor Staining buffer set (Thermo Fisher Scientific)
910 manufacturer's guidelines. When preparing samples for FACS sorting, NPCs were directly
911 blocked and stained with CD45-APC and CD31-BV421. Viability was evaluated by 7-AAD
912 (Biolegend) staining that was added to samples 5 min before sorting. Cell sorting was
913 performed on a BD FACSAria Fusion (BD Biosciences) equipped with four lasers: Blue (488
914 nm), Yellow/Green (561 nm), Red (640 nm) and Violet (405 nm). 85 μ m nozzle was used
915 and sheath fluid pressure was at 45 psi. A highly pure sorting modality (4-way purity sorting)
916 was chosen. The drop delay was determined using BD FACS AccuDrop beads. Unstained
917 and a single-stained controls have been used to set up compensation. Rainbow beads
918 (SPHEROTM Rainbow Calibration Particles) were used to standardize the experiment and
919 were run before each acquisition. Samples were sorted at 4°C to slow down metabolic
920 activities. Sorted cells were collected in 1.5 ml Eppendorf tubes containing 200 μ l of DMEM
921 10% FBS medium and immediately processed for RNA extraction using ReliaPrep™ RNA
922 Cell Miniprep System (Promega) and DNase TURBO (Thermo Fisher Scientific) following
923 manufacturer's recommendation.

924

925 **Isolation of HECs, including LSECs and splenic DCs for *in vitro* studies.** Mouse liver
 926 perfusion was performed as described in the section Electron Microscopy. After PBS
 927 perfusion, liver digestion was achieved *in situ* by perfusing warm digestion medium at 4 rpm
 928 for 10 min. The cava vein was squeezed tight several times to build up some pressure within
 929 the liver in order to fill all liver lobes with digestion medium. The resultant digested liver was
 930 excised, placed on a petri dish containing digestion medium and the Glisson's capsule was
 931 removed. Disaggregated tissue was filtered using a 70 µm cell strainer and centrifuged at
 932 50g for 3 min to discard hepatocytes. The supernatant containing NPCs was counted and
 933 Kupffer cells (KC) were removed using anti-F4/80 Ultrapure microbeads (Miltenyi Biotec)
 934 following manufacturer's guidelines. The flow-through of unlabeled NPCs was placed on top
 935 of a 25%-50% Percoll gradient and centrifuged at 850g for 20 min at RT without brake and
 936 the LSECs located at the 25/50% interface were collected. LSECs were counted and 10⁵
 937 cells were seeded in a 48-well plate and cultured in collagenated plates with EGM-2 medium
 938 (Lonza) for 3 days. For the isolation of splenic DC, spleens were slowly injected with 1ml of
 939 digestion medium until they changed from dark maroon to reddish-orange color. Then, the
 940 spleen was minced and pipetted vigorously several times in digestion medium. The cell
 941 suspension was filtered using a 70 µm cell strainer, and larger undigested fragments were
 942 ultimately incubated with digestion medium at 37°C for 30 min. After tissue digestion,
 943 splenocytes were centrifuged at 500 g for 5 min and washed 3 times with plain RPMI
 944 supplemented with 5mM EDTA to disrupt DC-T cell complexes. Red blood cells were lysed
 945 with ACK lysis buffer and DCs cells were isolated using anti-CD11c microbeads UltraPure
 946 (Miltenyi) according to manufacturer's instructions. CD11c⁺ DCs were counted and seeded
 947 at 10⁵ cells in a 48 well-plate using RPMI GlutaMAX supplemented with 10% FBS, 1% P/S,
 948 1x Na Pyruvate (Gibco), 1x MEM Non-essential Amino Acid Solution (Gibco), 20 µM β-
 949 mercaptoethanol and 40ng/ml GM-CSF (BioXcell). Every 48h 200 µl of fresh medium were

added to cultured cells and DCs were grown for 7 days to stimulate DCs differentiation.

Antigen cross-priming. Prior to naïve CD8⁺ T cell co-culture, HECs, including LSECs, and sDCs were stimulated for 18 h with 1 µg/ml of SIINFEKL peptide (OVA 257-264, Proimmune) or with 1 mg/ml of low endotoxin soluble ovalbumin protein (sOVA; Sigma-Aldrich) in combination with NaCl or 5 ng/ml of IFNα. Subsequently, after extensive washes, cells were co-culture with 5x10⁵ naïve CD8⁺T cells isolated from OT-I mice in complete RPMI (containing 10% FBS and 50 µM β-mercaptoethanol) in combination with NaCl or 5 ng/ml of IFNα. After 3 days, CD8⁺ T cells were stimulated for 4 h with 1 µg/ml of SIINFEKL peptide, 5 µg/ml of Brefeldin A (Sigma-Aldrich) and 2.5% EL-4 supernatant in complete RPMI. Finally, the production of IFNγ and the expression of activation markers, such as CD44, were measured by FACS.

RNA-seq and bioinformatic data analysis. RNA integrity, isolated from sorted liver CD31⁺ cells, was evaluated using the Agilent 4100 TapeStation (Agilent Technologies) and samples with RNA integrity number (RIN) above 7.0 were used for subsequent RNA-Seq-based profiling. Libraries were prepared using the Illumina Stranded mRNA ligation kit, according to the manufacturer's instructions. The RNA-Seq library was generated following the standard Illumina RNA-Seq protocol and sequenced on an Illumina NovaSeq 6000 machine (Illumina, San Diego, CA) obtaining an average of 40 million of single-end reads per sample. The raw reads produced from sequencing were trimmed using Trimmomatic, version 0.32, to remove adapters and to exclude low-quality reads from the analysis. The remaining reads were then aligned to the murine genome GRCm38 using STAR, version 2.5.3a. Reads were eventually assigned to the corresponding genomic features using featureCounts, according to the Gencode basic annotations (Gencode version M22). Quality of sequencing and alignment was assessed using FastQC, RseQC and MultiQC tools.

Expressed genes were defined as those genes showing at least 1 Count Per Million reads (CPM) on at least a selected number of samples, depending on the size of the compared groups (Chen *et al*, 2016). Low-expressed genes that did not match these criteria were excluded from the corresponding dataset. Gene expression read counts were exported and analyzed in R environment (v. 4.0.3) to identify differentially expressed genes (DEGs), using the DESeq2 Bioconductor library (v. 1.30.1, (Love *et al.*, 2014)). P-values were adjusted using a threshold for false discovery rate (FDR) < 0.05 (Benjamini & Hochberg, 1995). Significant genes were identified as those genes showing FDR < 0.05. Functional enrichment analysis was conducted using the enrichR R package (v. 3.0, (Kuleshov *et al*, 2016)), starting from the lists of differentially expressed genes as defined by FDR<0.05. Selected pathways were grouped and summarized according to their general biological functions and the hypergeometric test was performed to test the enrichment of these custom genesets, exploiting the hypeR R package (v. 1.8.0). Pre-ranked Gene Set Enrichment Analysis (GSEA (Subramanian *et al*, 2005)) was performed for each DGE comparison, on all the expressed genes ranked for Log2 fold change. The gene-sets included in the GSEA analyses were obtained from Canonical Pathways, Hallmark and the Gene Ontology collections as they are reported in the MSigDB database.

Statistical analysis. In all experiments values are expressed as mean values \pm SEM. Statistical significance was estimated by two-tailed non-parametric Mann-Whitney test (e.g. to evaluate differences generated as a consequence of tumor growth) or by one-way ANOVA with Tukey's multiple comparison test when more than two groups were analyzed. Contingency tables were tested by two-tailed Fisher's exact test and Chi-square test. Statistical significance of survival experiments was calculated by log-rank/Mantel-Cox test. All statistical analyses were performed with Prism 8 (GraphPad Software) and were reported in Figure legends. p-values <0.05 were considered statistically significant and reported on

graphs. If not mentioned, differences were not statistically significant.

Data and materials availability

Data for intrahepatic CD31 bulk RNA-seq is available in the Gene Expression Omnibus (GEO) database under the accession numbers GSE186203. Any additional information required to reanalyze the data reported in this paper is available upon request.

Acknowledgements

The authors thank B. Mendicino, C.B. Ekalle-Soppo, E. Daoud, P. Giangregorio, M. Nicoloso, M. Raso, A. Focchi, P. Marra, T. Canu, D. Lazarevic, E. Capitolo, S. Bianchessi, V. Berno, A. Raimondi, A. Loffreda, T. Catelani, M. Mainetti and P. Di Lucia for technical support; M. Silva for secretarial assistance, C. Tacchetti, P. Dellabona and all the San Raffaele AIRC 5X1000 team for helpful discussion. S.V. Kotenko for help with pSTAT1 IHC protocol. Confocal immunofluorescence histology and electron microscopy was carried out at Alembic, an advanced microscopy laboratory established by the San Raffaele Scientific Institute and the Vita-Salute San Raffaele University. The use of Imaris software was provided by M. Iannacone. Acquisition of SEM images was carried out at the Interdepartmental Microscopy Platform of the University of Milan Bicocca. Flow cytometry was carried out at FRACTAL, a flow cytometry resource and advanced cytometry technical applications laboratory established by the San Raffaele Scientific Institute. FRACTAL is an ISO 9001 certified facility and as such all the instruments and equipment are subject to a strict maintenance and functionality check plan. **Funding information:** N.L.T. is the recipient of a Swiss National Science Foundation Fellowship P2GEP3_171976; V.B. is the recipient of a Fondazione Umberto Veronesi “Post-doctoral Fellowships 2019”; A.M. is the recipient of a Francesco Fronzaroli Memorial fellowship and conducted this study as partial fulfilment of his PhD in Molecular Medicine within the program in Basic and Applied

Immunology and Oncology at Vita-Salute San Raffaele University. L.G.G. is supported by the Italian Association for Cancer Research (AIRC) Grant 22737, Lombardy Open Innovation Grant 229452, PRIN Grant 2017MPCWPY from the Italian Ministry of Education, University and Research, Funded Research Agreements from Gilead Sciences and Avalia Therapeutics; G.S. is supported by Italian Association for Cancer Research (AIRC) grants 18468, 22820 and AIRC 5 per Mille, grant 22737.

Author contributions

Conceptualization, G.S., N.L.T., L.M.F., and B.A.M.; Methodology, G.S., N.L.T., L.M.F., B.A.M., V.B., B.F., P.Z., A.M., C.F., E.B., G.M.S., R.L., C.G., and A.B.; Investigation, G.S., N.L.T., L.M.F., B.A.M., V.B., B.F., P.Z., A.M., and C.F.; Resources, G.S., A.B., and L.G.G.; Writing – original draft, G.S., N.L.T., L.M.F., and B.A.M.; Writing – Review & Editing, G.S., N.L.T., L.M.F., B.A.M., and L.G.G.; Visualization, G.S., N.L.T., L.M.F., B.A.M., and V.B.; Supervision, G.S., and A.E.; Project Administration, G.S.; Funding Acquisition, G.S., and L.G.G.

Conflict of interest

L.G.G is a member of the board of directors at Genenta Science and Epsilon Bio and participates in advisory boards/consultancies for Gilead Sciences, Roche, Arbutus Biopharma and Antios Therapeutics. All other authors have no additional financial interests.

References

- Aichele P, Unsoeld H, Koschella M, Schweier O, Kalinke U, Vucikuj S (2006) CD8 T cells specific for lymphocytic choriomeningitis virus require type I IFN receptor for clonal expansion. *Journal of immunology* 176: 4525-4529
- Ananth AA, Tai LH, Lansdell C, Alkayyal AA, Baxter KE, Angka L, Zhang J, Tanese de Souza C, Stephenson KB, Parato K *et al* (2016) Surgical Stress Abrogates Pre-Existing Protective T Cell Mediated Anti-Tumor Immunity Leading to Postoperative Cancer Recurrence. *PLoS one* 11: e0155947
- Argiles G, Tabernero J, Labianca R, Hochhauser D, Salazar R, Iveson T, Laurent-Puig P, Quirke P, Yoshino T, Taieb J *et al* (2020) Localised colon cancer: ESMO Clinical Practice Guidelines for diagnosis, treatment and follow-up. *Ann Oncol* 31: 1291-1305

Augustin G, Bruketa T, Korolija D, Milosevic M (2013) Lower incidence of hepatic metastases of colorectal cancer in patients with chronic liver diseases: meta-analysis. *Hepatogastroenterology* 60: 1164-1168

Badia-Ramentol J, Linares J, Gomez-Llonin A, Calon A (2021) Minimal Residual Disease, Metastasis and Immunity. *Biomolecules* 11

Baiocchi A, Del Nonno F, Taibi C, Visco-Comandini U, D'Offizi G, Piacentini M, Falasca L (2019) Liver sinusoidal endothelial cells (LSECs) modifications in patients with chronic hepatitis C. *Sci Rep* 9: 8760

Bakos O, Lawson C, Rouleau S, Tai LH (2018) Combining surgery and immunotherapy: turning an immunosuppressive effect into a therapeutic opportunity. *J Immunother Cancer* 6: 86

Benechet AP, De Simone G, Di Lucia P, Cilenti F, Barbiera G, Le Bert N, Fumagalli V, Lusito E, Moalli F, Bianchessi V *et al* (2019) Dynamics and genomic landscape of CD8(+) T cells undergoing hepatic priming. *Nature* 574: 200-205

Benjamini Y, Hochberg Y (1995) Controlling the False Discovery Rate: A Practical and Powerful Approach to Multiple Testing. *Journal of the Royal Statistical Society Series B (Methodological)* 57: 289-300

Bleriot C, Ginhoux F (2019) Understanding the Heterogeneity of Resident Liver Macrophages. *Front Immunol* 10: 2694

Bocci V (1994) Pharmacology and side-effects of interferons. *Antiviral Res* 24: 111-119

Bolger AM, Lohse M, Usadel B (2014) Trimmomatic: a flexible trimmer for Illumina sequence data. *Bioinformatics* 30: 2114-2120

Bottcher JP, Schanz O, Garbers C, Zaremba A, Hegenbarth S, Kurts C, Beyer M, Schultze JL, Kastenmuller W, Rose-John S *et al* (2014) IL-6 trans-signaling-dependent rapid development of cytotoxic CD8+ T cell function. *Cell Rep* 8: 1318-1327

Boukhaled GM, Harding S, Brooks DG (2021) Opposing Roles of Type I Interferons in Cancer Immunity. *Annu Rev Pathol* 16: 167-198

Brattain MG, Strobel-Stevens J, Fine D, Webb M, Sarraf AM (1980) Establishment of mouse colonic carcinoma cell lines with different metastatic properties. *Cancer research* 40: 2142-2146

Catarinella M, Monestiroli A, Escobar G, Focchi A, Tran NL, Aiolfi R, Marra P, Esposito A, Cipriani F, Aldrighetti L *et al* (2016) IFN α gene/cell therapy curbs colorectal cancer colonization of the liver by acting on the hepatic microenvironment. *EMBO Mol Med* 8: 155-170

Chambers AF, Groom AC, MacDonald IC (2002) Dissemination and growth of cancer cells in metastatic sites. *Nat Rev Cancer* 2: 563-572

Chen EY, Tan CM, Kou Y, Duan Q, Wang Z, Meirelles GV, Clark NR, Ma'ayan A (2013) Enrichr: interactive and collaborative HTML5 gene list enrichment analysis tool. *BMC Bioinformatics* 14: 128

Chen Y, Lun AT, Smyth GK (2016) From reads to genes to pathways: differential expression analysis of RNA-Seq experiments using Rsubread and the edgeR quasi-likelihood pipeline. *F1000Res* 5: 1438

Cheon H, Borden EC, Stark GR (2014) Interferons and their stimulated genes in the tumor microenvironment. *Semin Oncol* 41: 156-173

Chow FC, Chok KS (2019) Colorectal liver metastases: An update on multidisciplinary approach. *World J Hepatol* 11: 150-172

Cogger VC, O'Reilly JN, Warren A, Le Couteur DG (2015) A standardized method for the analysis of liver sinusoidal endothelial cells and their fenestrations by scanning electron microscopy. *J Vis Exp*: e52698

Crist SB, Ghajar CM (2021) When a House Is Not a Home: A Survey of Antimetastatic Niches and Potential Mechanisms of Disseminated Tumor Cell Suppression. *Annu Rev Pathol* 16: 409-432

Cunningham D, Atkin W, Lenz HJ, Lynch HT, Minsky B, Nordlinger B, Starling N (2010) Colorectal cancer. *Lancet* 375: 1030-1047

Curtsinger JM, Gerner MY, Lins DC, Mescher MF (2007) Signal 3 availability limits the CD8 T cell response to a solid tumor. *Journal of immunology* 178: 6752-6760

De Palma M, Mazziere R, Politi LS, Pucci F, Zonari E, Sitia G, Mazzoleni S, Moi D, Venneri MA, Indraccolo S *et al* (2008) Tumor-targeted interferon- α delivery by Tie2-expressing monocytes inhibits tumor growth and metastasis. *Cancer cell* 14: 299-311

Deneve E, Riethdorf S, Ramos J, Nocca D, Coffy A, Daures JP, Maudelonde T, Fabre JM, Pantel K, Alix-Panabieres C (2013) Capture of viable circulating tumor cells in the liver of colorectal cancer patients. *Clin Chem* 59: 1384-1392

Dobrzanski MJ, Reome JB, Dutton RW (2000) Type 1 and type 2 CD8⁺ effector T cell subpopulations promote long-term tumor immunity and protection to progressively growing tumor. *Journal of immunology* 164: 916-925

Efremova M, Rieder D, Klepsch V, Charoentong P, Finotello F, Hackl H, Hermann-Kleiter N, Lower M, Baier G, Krogsdam A *et al* (2018) Targeting immune checkpoints potentiates immunoediting and changes the dynamics of tumor evolution. *Nat Commun* 9: 32

Engstrand J, Stromberg C, Nilsson H, Freedman J, Jonas E (2019) Synchronous and metachronous liver metastases in patients with colorectal cancer-towards a clinically relevant definition. *World J Surg Oncol* 17: 228

Fioravanti J, Gonzalez I, Medina-Echeverez J, Larrea E, Ardaiz N, Gonzalez-Aseguinolaza G, Prieto J, Berraondo P (2011) Anchoring interferon alpha to apolipoprotein A-I reduces hematological toxicity while enhancing immunostimulatory properties. *Hepatology* 53: 1864-1873

Flanigan RC, Salmon SE, Blumenstein BA, Bearman SI, Roy V, McGrath PC, Caton JR, Jr., Munshi N, Crawford ED (2001) Nephrectomy followed by interferon alfa-2b compared with interferon alfa-2b alone for metastatic renal-cell cancer. *N Engl J Med* 345: 1655-1659

Foser S, Weyer K, Huber W, Certa U (2003) Improved biological and transcriptional activity of monopegylated interferon-alpha-2a isomers. *Pharmacogenomics J* 3: 312-319

Franciszkiewicz K, Boissonnas A, Boutet M, Combadiere C, Mami-Chouaib F (2012) Role of chemokines and chemokine receptors in shaping the effector phase of the antitumor immune response. *Cancer research* 72: 6325-6332

Fu C, Peng P, Loschko J, Feng L, Pham P, Cui W, Lee KP, Krug AB, Jiang A (2020) Plasmacytoid dendritic cells cross-prime naive CD8 T cells by transferring antigen to conventional dendritic cells through exosomes. *Proceedings of the National Academy of Sciences of the United States of America* 117: 23730-23741

Fuertes MB, Woo SR, Burnett B, Fu YX, Gajewski TF (2013) Type I interferon response and innate immune sensing of cancer. *Trends Immunol* 34: 67-73

Gerl K, Miquerol L, Todorov VT, Hugo CP, Adams RH, Kurtz A, Kurt B (2015) Inducible glomerular erythropoietin production in the adult kidney. *Kidney Int* 88: 1345-1355

Gessani S, Conti L, Del Corno M, Belardelli F (2014) Type I interferons as regulators of human antigen presenting cell functions. *Toxins (Basel)* 6: 1696-1723

Gissen P, Arias IM (2015) Structural and functional hepatocyte polarity and liver disease. *J Hepatol* 63: 1023-1037

Glinskii OV, Huxley VH, Glinsky GV, Pienta KJ, Raz A, Glinsky VV (2005) Mechanical entrapment is insufficient and intercellular adhesion is essential for metastatic cell arrest in distant organs. *Neoplasia* 7: 522-527

Glue P, Rouzier-Panis R, Raffanel C, Sabo R, Gupta SK, Salfi M, Jacobs S, Clement RP (2000) A dose-ranging study of pegylated interferon alfa-2b and ribavirin in chronic hepatitis C. The Hepatitis C Intervention Therapy Group. *Hepatology* 32: 647-653

Guidotti LG, Inverso D, Sironi L, Di Lucia P, Fioravanti J, Ganzer L, Fiocchi A, Vacca M, Aiolfi R, Sammiceli S *et al* (2015) Immunosurveillance of the liver by intravascular effector CD8⁺ T cells. *Cell* 161: 486-500

Gul N, Bogels M, Grewal S, van der Meer AJ, Rojas LB, Fluitsma DM, van den Tol MP, Hoebe KA, van Marle J, de Vries HE *et al* (2011) Surgery-induced reactive oxygen species enhance colon carcinoma cell binding by disrupting the liver endothelial cell lining. *Gut* 60: 1076-1086

Herndon TM, Demko SG, Jiang X, He K, Gootenberg JE, Cohen MH, Keegan P, Pazdur R (2012) U.S. Food and Drug Administration Approval: peginterferon-alfa-2b for the adjuvant treatment of patients with melanoma. *Oncologist* 17: 1323-1328

Horowitz M, Neeman E, Sharon E, Ben-Eliyahu S (2015) Exploiting the critical perioperative period to improve long-term cancer outcomes. *Nature reviews Clinical oncology* 12: 213-226

Inagawa R, Okada H, Takemura G, Suzuki K, Takada C, Yano H, Ando Y, Usui T, Hotta Y, Miyazaki N *et al* (2018) Ultrastructural Alteration of Pulmonary Capillary Endothelial Glycocalyx During Endotoxemia. *Chest* 154: 317-325

Indraccolo S (2010) Interferon-alpha as angiogenesis inhibitor: learning from tumor models. *Autoimmunity* 43: 244-247

Jacobs F, Wisse E, De Geest B (2010) The role of liver sinusoidal cells in hepatocyte-directed gene transfer. *Am J Pathol* 176: 14-21

Jeon S, Juhn JH, Han S, Lee J, Hong T, Paek J, Yim DS (2013) Saturable human neopterin response to interferon-alpha assessed by a pharmacokinetic-pharmacodynamic model. *Journal of translational medicine* 11: 240

Karmaus PW, Chi H (2014) Genetic dissection of dendritic cell homeostasis and function: lessons from cell type-specific gene ablation. *Cell Mol Life Sci* 71: 1893-1906

Katliniski KV, Gui J, Katlinskaya YV, Ortiz A, Chakraborty R, Bhattacharya S, Carbone CJ, Beiting DP, Gironde MA, Peck AR *et al* (2017) Inactivation of Interferon Receptor Promotes the Establishment of Immune Privileged Tumor Microenvironment. *Cancer cell* 31: 194-207

Katz SC, Pillarisetty VG, Bleier JI, Shah AB, DeMatteo RP (2004) Liver sinusoidal endothelial cells are insufficient to activate T cells. *Journal of immunology* 173: 230-235

Klebanoff CA, Gattinoni L, Torabi-Parizi P, Kerstann K, Cardones AR, Finkelstein SE, Palmer DC, Antony PA, Hwang ST, Rosenberg SA *et al* (2005) Central memory self/tumor-reactive CD8+ T cells confer superior antitumor immunity compared with effector memory T cells. *Proceedings of the National Academy of Sciences of the United States of America* 102: 9571-9576

Kohne CH, Wilke H, Hiddemann W, Bokemeyer C, Lohrmann HP, Bodenstein H, Preiss J, Rauschecker H, Hill H, Kaufer C *et al* (1997) Phase II evaluation of 5-fluorouracil plus folinic acid and alpha 2b-interferon in metastatic colorectal cancer. *Oncology* 54: 96-101

Kondo T, Okabayashi K, Hasegawa H, Tsuruta M, Shigeta K, Kitagawa Y (2016) The impact of hepatic fibrosis on the incidence of liver metastasis from colorectal cancer. *Br J Cancer* 115: 34-39

Kuleshov MV, Jones MR, Rouillard AD, Fernandez NF, Duan Q, Wang Z, Koplev S, Jenkins SL, Jagodnik KM, Lachmann A *et al* (2016) Enrichr: a comprehensive gene set enrichment analysis web server 2016 update. *Nucleic Acids Res* 44: W90-97

Lens MB, Dawes M (2002) Interferon alfa therapy for malignant melanoma: a systematic review of randomized controlled trials. *Journal of clinical oncology : official journal of the American Society of Clinical Oncology* 20: 1818-1825

Li Destri G, Castaing M, Ferlito F, Minutolo V, Di Cataldo A, Puleo S (2013) Rare hepatic metastases of colorectal cancer in livers with symptomatic HBV and HCV hepatitis. *Annali italiani di chirurgia* 84: 323-327

Li Z, Zhu Y, Li C, Trinh R, Ren X, Sun F, Wang Y, Shang P, Wang T, Wang M *et al* (2017) Anti-VEGFR2-interferon-alpha2 regulates the tumor microenvironment and exhibits potent antitumor efficacy against colorectal cancer. *Oncoimmunology* 6: e1290038

Liang Y, Tang H, Guo J, Qiu X, Yang Z, Ren Z, Sun Z, Bian Y, Xu L, Xu H *et al* (2018) Targeting IFNalpha to tumor by anti-PD-L1 creates feedforward antitumor responses to overcome checkpoint blockade resistance. *Nat Commun* 9: 4586

Lin JD, Feng N, Sen A, Balan M, Tseng HC, McElrath C, Smirnov SV, Peng J, Yasukawa LL, Durbin RK *et al* (2016) Distinct Roles of Type I and Type III Interferons in Intestinal Immunity to Homologous and Heterologous Rotavirus Infections. *PLoS pathogens* 12: e1005600

Link KH, Kornmann M, Staib L, Redenbacher M, Kron M, Beger HG, Study Group Oncology of Gastrointestinal T (2005) Increase of survival benefit in advanced resectable colon cancer by extent of adjuvant treatment: results of a randomized trial comparing modulation of 5-FU + levamisole with folinic acid or with interferon-alpha. *Annals of surgery* 242: 178-187

Liu W, Hou Y, Chen H, Wei H, Lin W, Li J, Zhang M, He F, Jiang Y (2011) Sample preparation method for isolation of single-cell types from mouse liver for proteomic studies. *Proteomics* 11: 3556-3564

Love MI, Huber W, Anders S (2014) Moderated estimation of fold change and dispersion for RNA-seq data with DESeq2. *Genome Biol* 15: 550

Madisen L, Zwingman TA, Sunkin SM, Oh SW, Zariwala HA, Gu H, Ng LL, Palmiter RD, Hawrylycz MJ, Jones AR *et al* (2010) A robust and high-throughput Cre reporting and characterization system for the whole mouse brain. *Nat Neurosci* 13: 133-140

Mak KM, Mei R (2017) Basement Membrane Type IV Collagen and Laminin: An Overview of Their Biology and Value as Fibrosis Biomarkers of Liver Disease. *Anat Rec (Hoboken)* 300: 1371-1390

Mitchell MJ, King MR (2014) Physical biology in cancer. 3. The role of cell glycocalyx in vascular transport of circulating tumor cells. *Am J Physiol Cell Physiol* 306: C89-97

Montoya M, Schiavoni G, Mattei F, Gresser I, Belardelli F, Borrow P, Tough DF (2002) Type I interferons produced by dendritic cells promote their phenotypic and functional activation. *Blood* 99: 3263-3271

Offeddu GS, Hajal C, Foley CR, Wan Z, Ibrahim L, Coughlin MF, Kamm RD (2021) The cancer glycocalyx mediates intravascular adhesion and extravasation during metastatic dissemination. *Commun Biol* 4: 255

Pandey E, Nour AS, Harris EN (2020) Prominent Receptors of Liver Sinusoidal Endothelial Cells in Liver Homeostasis and Disease. *Front Physiol* 11: 873

Park CG, Hartl CA, Schmid D, Carmona EM, Kim HJ, Goldberg MS (2018) Extended release of perioperative immunotherapy prevents tumor recurrence and eliminates metastases. *Science translational medicine* 10

Pavlovic Z, Risovic D, Novakovic D (2012) Comparative study of direct and indirect image-based profilometry in characterization of surface roughness. *Surf Interface Anal* 44: 825-830

Postic C, Shiota M, Niswender KD, Jetton TL, Chen Y, Moates JM, Shelton KD, Lindner J, Cherrington AD, Magnuson MA (1999) Dual roles for glucokinase in glucose homeostasis as determined by liver and pancreatic beta cell-specific gene knock-outs using Cre recombinase. *J Biol Chem* 274: 305-315

Prigge JR, Hoyt TR, Dobrinen E, Capecchi MR, Schmidt EE, Meissner N (2015) Type I IFNs Act upon Hematopoietic Progenitors To Protect and Maintain Hematopoiesis during Pneumocystis Lung Infection in Mice. *Journal of immunology* 195: 5347-5357

Reitsma S, Slaaf DW, Vink H, van Zandvoort MA, oude Egbrink MG (2007) The endothelial glycocalyx: composition, functions, and visualization. *Pflugers Arch* 454: 345-359

Rodriguez A, Regnault A, Kleijmeer M, Ricciardi-Castagnoli P, Amigorena S (1999) Selective transport of internalized antigens to the cytosol for MHC class I presentation in dendritic cells. *Nat Cell Biol* 1: 362-368

Rosenberg SA, Spiess P, Lafreniere R (1986) A new approach to the adoptive immunotherapy of cancer with tumor-infiltrating lymphocytes. *Science* 233: 1318-1321

Sallusto F, Geginat J, Lanzavecchia A (2004) Central memory and effector memory T cell subsets: function, generation, and maintenance. *Annu Rev Immunol* 22: 745-763

Sargent D, Sobrero A, Grothey A, O'Connell MJ, Buyse M, Andre T, Zheng Y, Green E, Labianca R, O'Callaghan C *et al* (2009) Evidence for cure by adjuvant therapy in colon cancer: observations based on individual patient data from 20,898 patients on 18 randomized trials. *Journal of clinical oncology : official journal of the American Society of Clinical Oncology* 27: 872-877

Schindelin J, Arganda-Carreras I, Frise E, Kaynig V, Longair M, Pietzsch T, Preibisch S, Rueden C, Saalfeld S, Schmid B *et al* (2012) Fiji: an open-source platform for biological-image analysis. *Nature methods* 9: 676-682

Schreiber G (2017) The molecular basis for differential type I interferon signaling. *J Biol Chem* 292: 7285-7294

Seo SI, Lim SB, Yoon YS, Kim CW, Yu CS, Kim TW, Kim JH, Kim JC (2013) Comparison of recurrence patterns between ≤ 5 years and > 5 years after curative operations in colorectal cancer patients. *Journal of surgical oncology* 108: 9-13

Sitia G, Aiolfi R, Di Lucia P, Mainetti M, Fiocchi A, Mingozzi F, Esposito A, Ruggeri ZM, Chisari FV, Iannacone M *et al* (2012) Antiplatelet therapy prevents hepatocellular carcinoma and improves survival in a mouse model of chronic hepatitis B. *Proceedings of the National Academy of Sciences of the United States of America* 109: E2165-2172

Sitia G, Iannacone M, Aiolfi R, Isogawa M, van Rooijen N, Scozzesi C, Bianchi ME, von Andrian UH, Chisari FV, Guidotti LG (2011) Kupffer cells hasten resolution of liver immunopathology in mouse models of viral hepatitis. *PLoS pathogens* 7: e1002061

Sorensen KK, Smedsrod, B. (2020) The Liver Sinusoidal Endothelial Cell: Basic Biology and Pathobiology. In: *The Liver: Biology and Pathobiology, Sixth Edition* pp. 422-434. John Wiley & Sons Ltd. :

Stewart SA, Dominguez-Robles J, Donnelly RF, Larraneta E (2018) Implantable Polymeric Drug Delivery Devices: Classification, Manufacture, Materials, and Clinical Applications. *Polymers (Basel)* 10

Stone JD, Chervin AS, Kranz DM (2009) T-cell receptor binding affinities and kinetics: impact on T-cell activity and specificity. *Immunology* 126: 165-176

Su T, Yang Y, Lai S, Jeong J, Jung Y, McConnell M, Utsumi T, Iwakiri Y (2021) Single-Cell Transcriptomics Reveals Zone-Specific Alterations of Liver Sinusoidal Endothelial Cells in Cirrhosis. *Cell Mol Gastroenterol Hepatol* 11: 1139-1161

Subramanian A, Tamayo P, Mootha VK, Mukherjee S, Ebert BL, Gillette MA, Paulovich A, Pomeroy SL, Golub TR, Lander ES *et al* (2005) Gene set enrichment analysis: a knowledge-based approach for interpreting genome-wide expression profiles. *Proceedings of the National Academy of Sciences of the United States of America* 102: 15545-15550

Sung H, Ferlay J, Siegel RL, Laversanne M, Soerjomataram I, Jemal A, Bray F (2021) Global cancer statistics 2020: GLOBOCAN estimates of incidence and mortality worldwide for 36 cancers in 185 countries. *CA Cancer J Clin*

Talamini L, Picchetti P, Ferreira LM, Sitia G, Russo L, Violatto MB, Travaglini L, Fernandez Alarcon J, Righelli L, Bigini P *et al* (2021) Organosilica Cages Target Hepatic Sinusoidal Endothelial Cells Avoiding Macrophage Filtering. *ACS Nano*

Tanjore H, Kalluri R (2006) The role of type IV collagen and basement membranes in cancer progression and metastasis. *Am J Pathol* 168: 715-717

Tauriello DVF, Palomo-Ponce S, Stork D, Berenguer-Llargo A, Badia-Ramentol J, Iglesias M, Sevillano M, Ibiza S, Canellas A, Hernando-Momblona X *et al* (2018) TGFbeta drives immune evasion in genetically reconstituted colon cancer metastasis. *Nature* 554: 538-543

Tirone M, Tran NL, Ceriotti C, Gorzanelli A, Canepari M, Bottinelli R, Raucci A, Di Maggio S, Santiago C, Mellado M *et al* (2018) High mobility group box 1 orchestrates tissue regeneration via CXCR4. *The Journal of experimental medicine* 215: 303-318

Toyoshima Y, Kitamura H, Xiang H, Ohno Y, Homma S, Kawamura H, Takahashi N, Kamiyama T, Tanino M, Taketomi A (2019) IL6 Modulates the Immune Status of the Tumor Microenvironment to Facilitate Metastatic Colonization of Colorectal Cancer Cells. *Cancer Immunol Res* 7: 1944-1957

Valastyan S, Weinberg RA (2011) Tumor metastasis: molecular insights and evolving paradigms. *Cell* 147: 275-292

van der Bij GJ, Bogels M, Otten MA, Oosterling SJ, Kuppen PJ, Meijer S, Beelen RH, van Egmond M (2010) Experimentally induced liver metastases from colorectal cancer can be prevented by mononuclear phagocyte-mediated monoclonal antibody therapy. *J Hepatol* 53: 677-685

van Gestel YR, de Hingh IH, van Herk-Sukel MP, van Erning FN, Beerepoot LV, Wijsman JH, Slooter GD, Rutten HJ, Creemers GJ, Lemmens VE (2014) Patterns of metachronous metastases after curative treatment of colorectal cancer. *Cancer Epidemiol* 38: 448-454

Wang Y, Nakayama M, Pitulescu ME, Schmidt TS, Bochenek ML, Sakakibara A, Adams S, Davy A, Deutsch U, Luthi U *et al* (2010) Ephrin-B2 controls VEGF-induced angiogenesis and lymphangiogenesis. *Nature* 465: 483-486

Warren A, Bertolino P, Benseler V, Fraser R, McCaughan GW, Le Couteur DG (2007) Marked changes of the hepatic sinusoid in a transgenic mouse model of acute immune-mediated hepatitis. *J Hepatol* 46: 239-246

Weber JS, Yang JC, Atkins MB, Disis ML (2015) Toxicities of Immunotherapy for the Practitioner. *Journal of clinical oncology : official journal of the American Society of Clinical Oncology* 33: 2092-2099

Wilkinson AL, Qurashi M, Shetty S (2020) The Role of Sinusoidal Endothelial Cells in the Axis of Inflammation and Cancer Within the Liver. *Front Physiol* 11: 990

Winkler M, Staniczek T, Kurschner SW, Schmid CD, Schonhaber H, Cordero J, Kessler L, Mathes A, Sticht C, Nessling M *et al* (2021) Endothelial GATA4 controls liver fibrosis and regeneration by preventing a pathogenic switch in angiocrine signaling. *J Hepatol* 74: 380-393

Wohlfeil SA, Hafele V, Dietsch B, Schledzewski K, Winkler M, Zierow J, Leibing T, Mohammadi MM, Heineke J, Sticht C *et al* (2019) Hepatic Endothelial Notch Activation Protects against Liver Metastasis by Regulating Endothelial-Tumor Cell Adhesion Independent of Angiocrine Signaling. *Cancer research* 79: 598-610

Wolf MJ, Hoos A, Bauer J, Boettcher S, Knust M, Weber A, Simonavicius N, Schneider C, Lang M, Sturzl M *et al* (2012) Endothelial CCR2 signaling induced by colon carcinoma cells enables extravasation via the JAK2-Stat5 and p38MAPK pathway. *Cancer cell* 22: 91-105

Yang X, Zhang X, Fu ML, Weichselbaum RR, Gajewski TF, Guo Y, Fu Y-X, 2014. Targeting the Tumor Microenvironment with Interferon- γ ; Bridges Innate and Adaptive Immune Responses, *Cancer cell*. Elsevier Inc., pp. 37-48.

Yu X, Chen L, Liu J, Dai B, Xu G, Shen G, Luo Q, Zhang Z (2019) Immune modulation of liver sinusoidal endothelial cells by melittin nanoparticles suppresses liver metastasis. *Nat Commun* 10: 574

Yun S, Huang JJ (2016) Routes for Drug Delivery: Sustained-Release Devices. *Dev Ophthalmol* 55: 84-92

Zhang Y, Davis C, Ryan J, Janney C, Pena MM (2013) Development and characterization of a reliable mouse model of colorectal cancer metastasis to the liver. *Clin Exp Metastasis* 30: 903-918

Figures

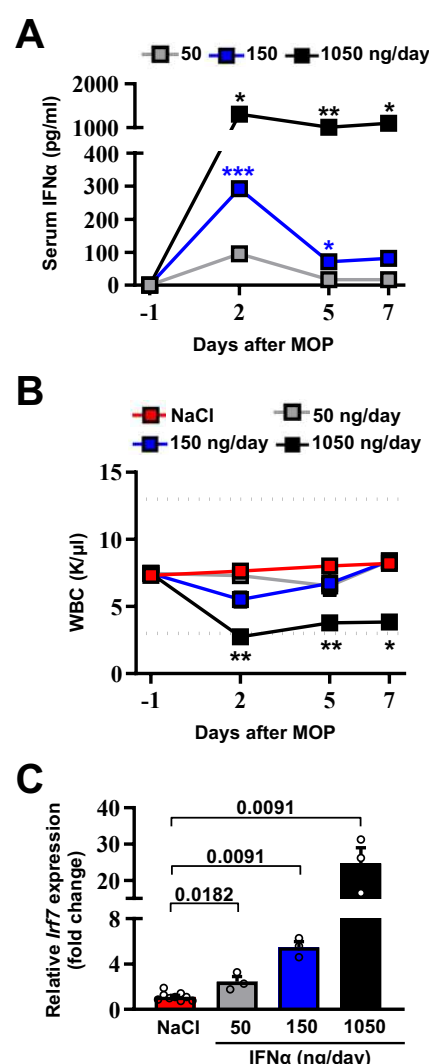


Figure 1. Selection of the optimal IFNα dosing regimen. (A) Quantification of plasma IFNα concentration from mice continuously treated with different IFNα doses at the indicated time points. Mean values ± SEM are shown; p-values were calculated by one-way ANOVA Tukey's multiple comparison test. Significant p-values refer to the IFNα 50 ng/day group, since NaCl-treated animals had IFNα plasma levels below the assay detection limit. $p \leq 0.05$; $**p \leq 0.01$; $***p \leq 0.001$. (B) White blood cell (WBC) counts of mice treated with different IFNα doses at indicated time points. Horizontal dashed lines delimit normal WBC range. Mean value ± SEM are shown; p-values were calculated by one-way ANOVA Tukey's multiple comparison test. Significant p-values are referred to the NaCl group. $*p \leq 0.05$; $**p \leq 0.01$. (C) Quantitative real-time PCR analysis of *Ifi7* mRNA expression from liver tissues of mice treated with different IFNα doses for 7 days. Basal *Ifi7* mRNA expression level was determined in control mice (NaCl; n=9) and the relative expression of *Ifi7* upon IFNα treatment is shown (n=3, for each IFNα-treated group). Mean values ± SEM are shown; p-values were calculated by one-way ANOVA Tukey's multiple comparison test.

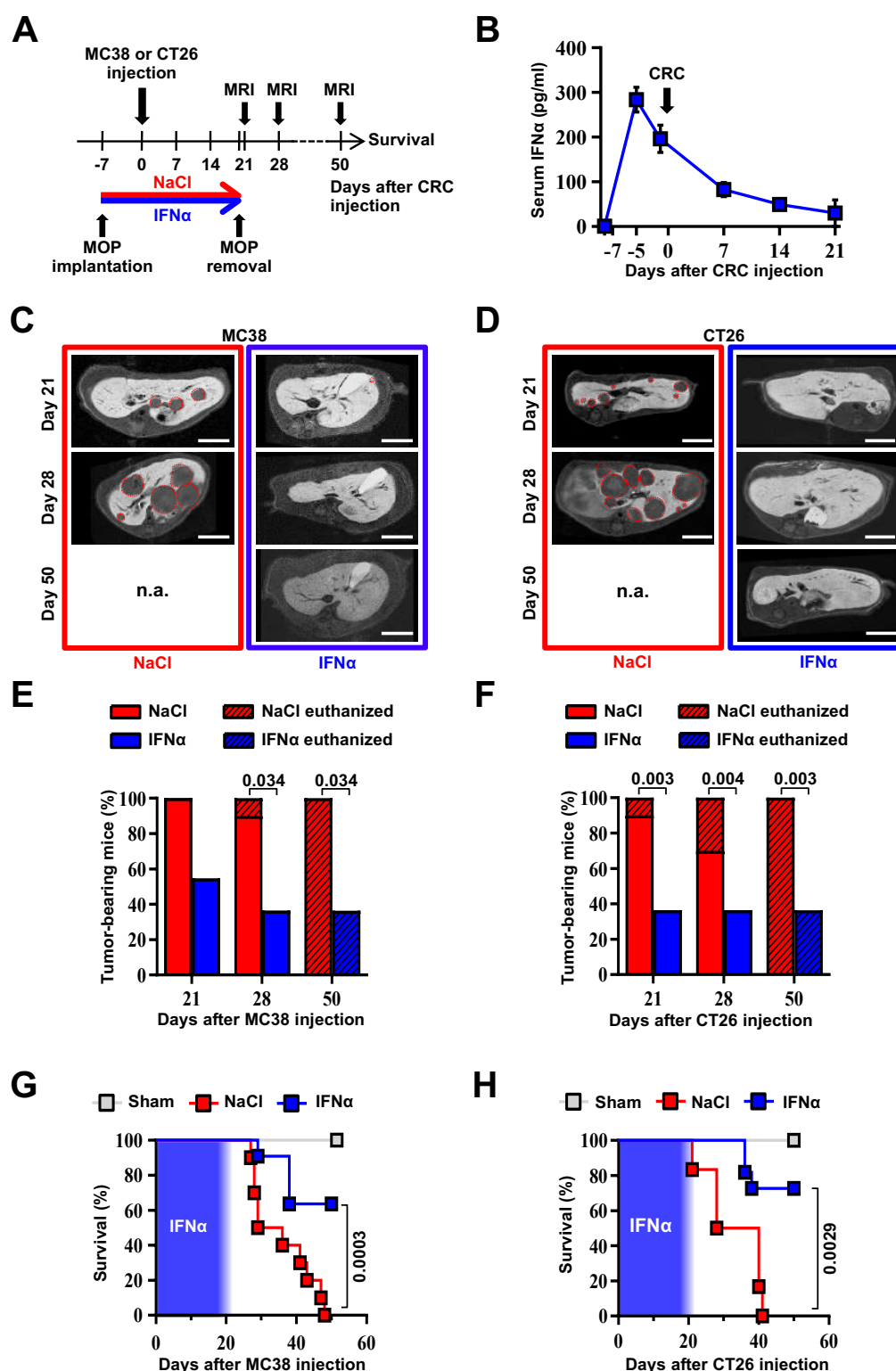


Figure 2. Continuous IFN α administration reduces liver CRC metastatic burden and improves survival. (A) Schematic representation of the experimental procedure. Intrasplenic injection of 7×10^4 MC38 or 5×10^3 CT26 cells was performed 7 days after continuous NaCl or IFN α therapy. (B) Quantification of plasma IFN α concentration at different time points after continuous IFN α administration (n=6). The time of intrasplenic CRC cell injection has also been depicted. Mean values \pm SEM are shown. (C-D) Representative T1 contrast-enhanced magnetic resonance images (MRI) of the liver of mice treated with NaCl (red frame) and IFN α (blue frame) at 21, 28 and 50 days after MC38 (C) or CT26 (D) cells injection. Red dashed lines highlight CRC liver metastases, characterized as hypointense regions in T1-weighted sequences. n.a.=not assessed, is referred to mice euthanized before the specified time point; scale bar=5mm. (E-F) Percentage of mice treated with NaCl (MC38 n=3+3; CT26 n=5+5 for each of two independent experiments) or IFN α (MC38 n=5+6; CT26 n=5+6 for each of two independent experiments) bearing at least one CRC liver metastasis estimated by MRI.

analysis at indicated time points after MC38 or CT26 injection. The oblique black line pattern within columns depicts the percentage of mice euthanized before the indicated time point. Mean values are shown; p-values were calculated by Fisher's exact test. **(G-H)** Kaplan-Meier survival curves of Sham (n=3), NaCl- (MC38 n=6; CT26 n=10) or IFN α -treated (MC38 n=11; CT26 n=11) mice after MC38 or CT26 cells injection. The blue pattern indicates the time frame of IFN α ip release; p-values were calculated by log-rank/Mantel-Cox test.

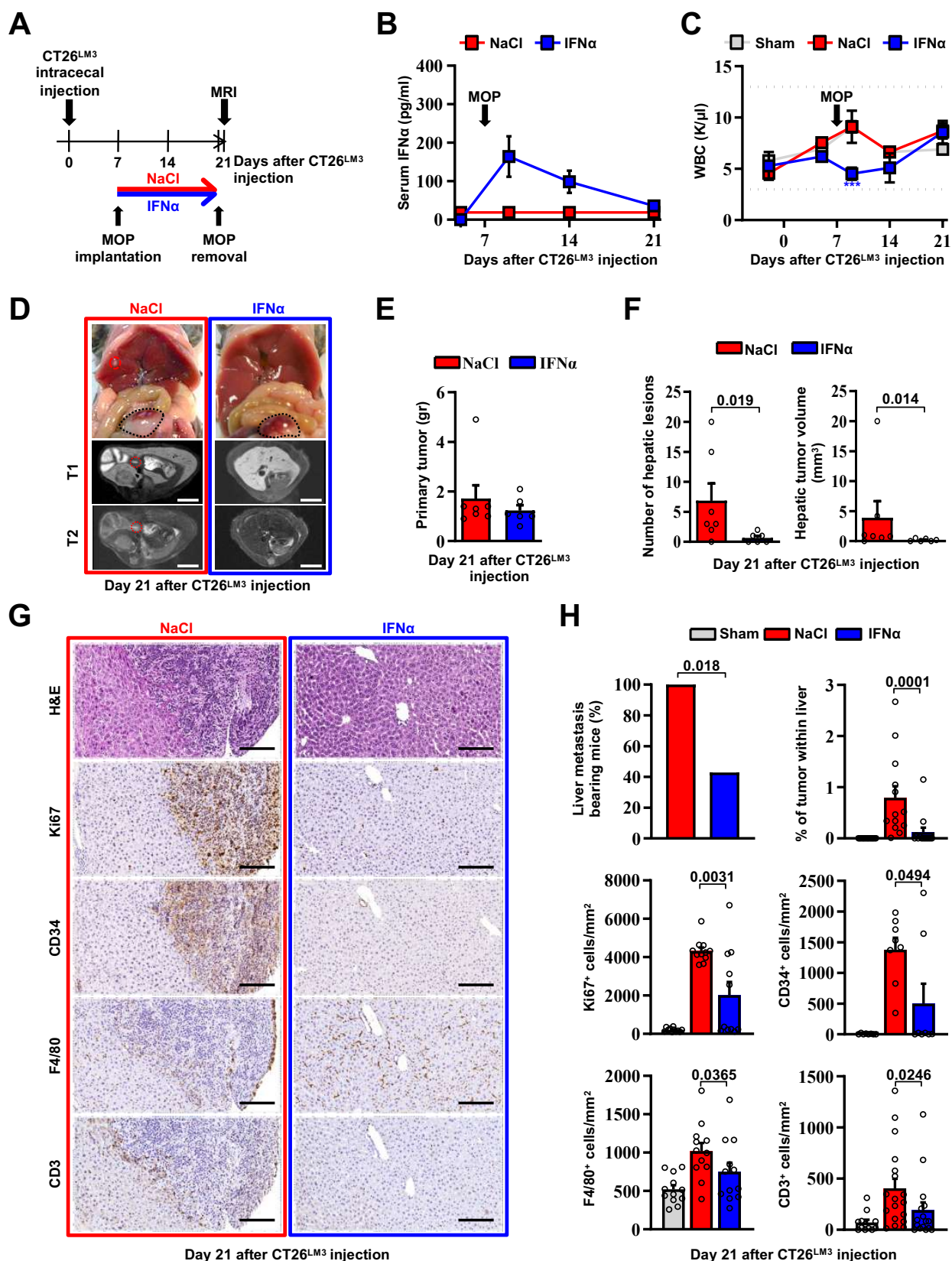


Figure 3. Continuous IFN α administration prevents spontaneous hepatic colonization of orthotopically implanted CT26^{LM3} cells. (A) Schematic representation of the experimental procedure. Seven days after intracecal injection of 2×10^5 CT26^{LM3} cells, mice were randomly assigned to receive either continuous NaCl (n=7) or IFN α (n=6) administration and analyzed by MRI 14 days later. (B) Quantification of plasma IFN α concentration at the indicated time point after cecal wall injection of CT26^{LM3} cells in mice described in a. The arrow indicates the time of NaCl or IFN α therapy initiation. Mean values \pm SEM are shown. (C) WBC counts from mice described in (A) continuously treated with NaCl or IFN α at indicated time points. Horizontal dashed

lines delimit the normal WBC range. The time of MOP implantation has also been depicted. Mean value \pm SEM are shown; p-values were calculated by one-way ANOVA Tukey's multiple comparison test. Significant p-values are referred to NaCl group. *** $p \leq 0.001$. **(D)** Representative images (top panels) of the hepatic lesions and intracecal tumors observed in NaCl- (red frame) and IFN α -treated (blue frame) mice, 21 days after CT26^{LM3} cells intracecal wall injection, and the corresponding hepatic contrast-enhanced MRI, T1-weighted (middle panels) and T2-weighted (bottom panels) sequences. Red dashed lines identify macroscopic liver metastatic lesions. Scale bars=5mm. **(E)** Quantification of the weight of primary CRC tumors 21 days after CT26^{LM3} cells intracecal wall injection of mice described in D. **(F)** Quantification of the number of hepatic lesions and total tumor volume of liver metastases by MRI analysis of mice described in D. Mean values \pm SEM are shown; p-values were calculated by Mann-Whitney test. **(G)** Representative H&E, Ki67, CD34, F4/80 and CD3 immunohistochemical micrographs of liver metastatic lesions found in NaCl- (red frame) and IFN α -treated (blue frame) mice, 21 days after intracecal injection of CT26^{LM3} cells. Scale bar=100 μ m. **(H)** Quantification of the percentage of mice bearing liver metastases, as well as the percentage of tumor area and the number of cells expressing Ki67, CD34, F4/80 and CD3 per mm² determined by IHC. Immunohistochemical measurements were conducted on at least 1000 mm² of total liver area for both experimental conditions. Mean values \pm SEM are shown; p-values were calculated by Mann-Whitney test.

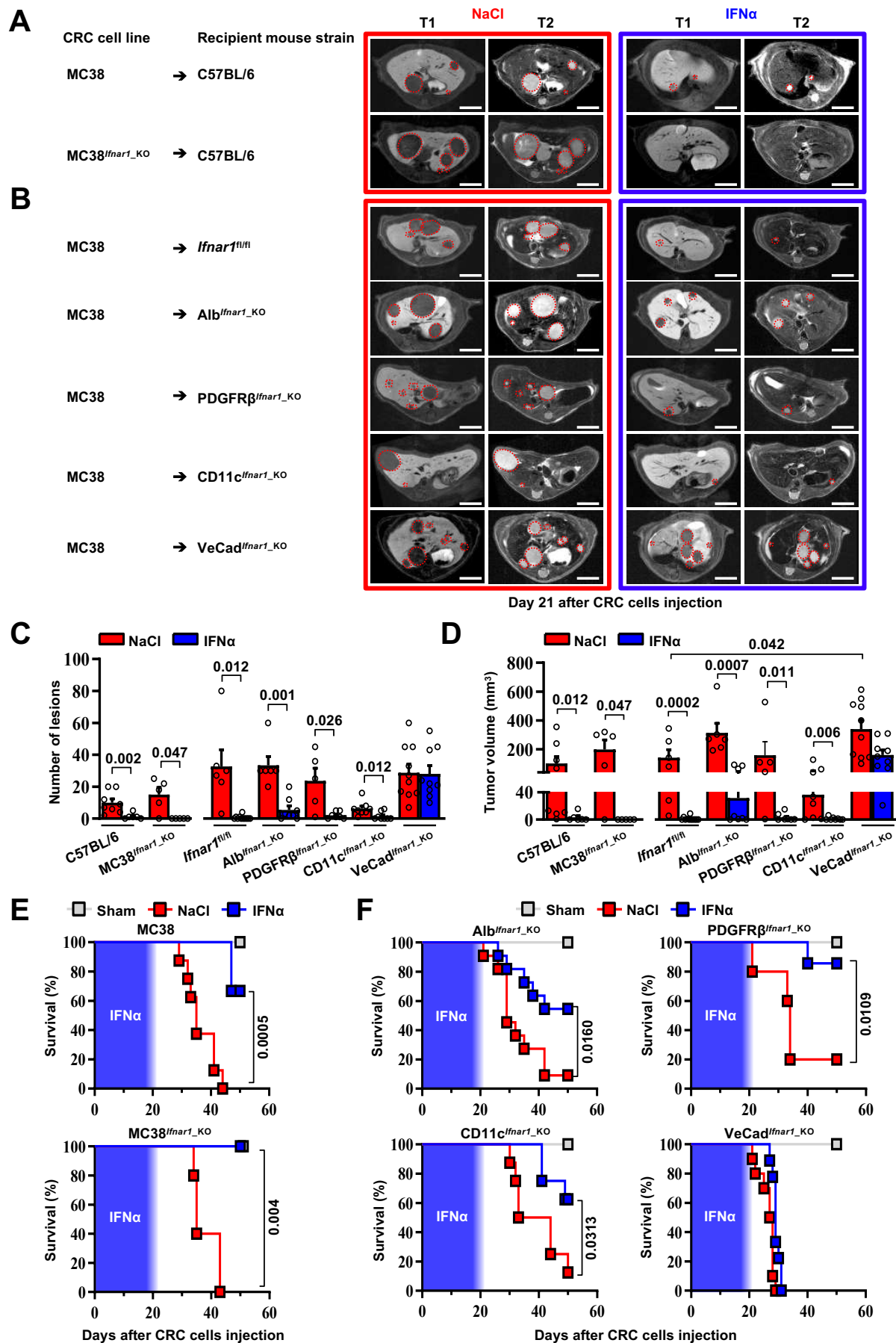


Figure 4. HECs mediate the antimetastatic activity of IFN α . (A) Representative hepatic contrast-enhanced MRI of wild-type mice (C57BL/6) at day 21 after injection of 5×10^4 MC38 cells or 5×10^4 MC38^{Ifnar1_KO} cells. Treatment with NaCl (red frame) and IFN α (blue frame) was initiated 7 days prior to intrasplenic injection of

CRC cells. Red dashed lines highlight CRC liver metastases, characterized as hypointense and slightly-hyperintense regions in T1- and T2-weighted sequences, respectively. Scale bar=5mm. The number of mice for each experimental condition is also indicated. **(B)** Representative hepatic contrast-enhanced MRI at day 21 after MC38 intrasplenic injection of *Ifnar1^{fl/fl}* mice and mice lacking *Ifnar1* on hepatocytes (*Alb^{Ifnar1_KO}*), hepatic stellate cells (*PDGFRβ^{Ifnar1_KO}*), CD11c-expressing DCs/KCs/LMCs (*CD11c^{Ifnar1_KO}*) and endothelial cells (*VeCad^{Ifnar1_KO}*) injected with 5×10^4 MC38 cells. Treatment with NaCl (red frame) and IFNα (blue frame) was initiated 7 days before MC38 cells intrasplenic injection. Red dashed lines highlight CRC liver metastases, characterized as hypointense and slightly-hyperintense regions in T1- and T2-weighted sequences, respectively. Scale bar=5mm. Number of mice for each experimental condition are also indicated. **(C)** Quantification of the number of hepatic lesions by MRI analysis, 21 days after CRC cells injection, of NaCl and IFNα-treated mice found in C57BL/6 mice, *Ifnar1^{fl/fl}* mice and all conditional *Ifnar1_KO* mouse models described in **(A)** and **(B)**. Mean values \pm SEM are shown; p-values were calculated by Mann-Whitney test. **(D)** Quantification of total tumor volume of liver metastases by MRI analysis at day 21 after CRC intrasplenic injection of NaCl- and IFNα-treated mice found in C57BL/6 mice, *Ifnar1^{fl/fl}* mice and all conditional *Ifnar1_KO* mouse models analyzed. Mean values \pm SEM are shown; p-values were calculated by Mann-Whitney test. **(E)** Kaplan-Meier survival curves of C57BL/6 mice injected with MC38 cells (top) or MC38^{*Ifnar1_KO*} cells (bottom) described in **(A)**. Sham injected animals (n=3) were used as control. The blue pattern indicates the time frame of IFNα ip release; p-values were calculated by log-rank/Mantel-Cox test. **(F)** Kaplan-Meier survival curves of the indicated groups of mice described in **(B)**. Sham injected animals (n=3 per group) were used as control. The blue pattern indicates the time frame of IFNα ip release. The total number of mice for each experimental group were: NaCl-C57BL/6 n=8; IFNα-C57BL/6 n=6; NaCl-MC38^{*Ifnar1_KO*}-C57BL/6 n=5; IFNα-MC38^{*Ifnar1_KO*}-C57BL/6 n=6; NaCl-*Ifnar1^{fl/fl}* n=6; IFNα-*Ifnar1^{fl/fl}* n=11; NaCl-*Alb^{Ifnar1_KO}* n=6; IFNα-*Alb^{Ifnar1_KO}* n=8; NaCl-*PDGFRβ^{Ifnar1_KO}* n=5; IFNα-*PDGFRβ^{Ifnar1_KO}* n=7; NaCl-*CD11c^{Ifnar1_KO}* n=8; IFNα-*CD11c^{Ifnar1_KO}* n=8 and NaCl-*VeCad^{Ifnar1_KO}* n=10; IFNα-*VeCad^{Ifnar1_KO}* n=9. Data pooled from at least 2 independent experiments of each experimental group; p-values were calculated by log-rank/Mantel-Cox test.

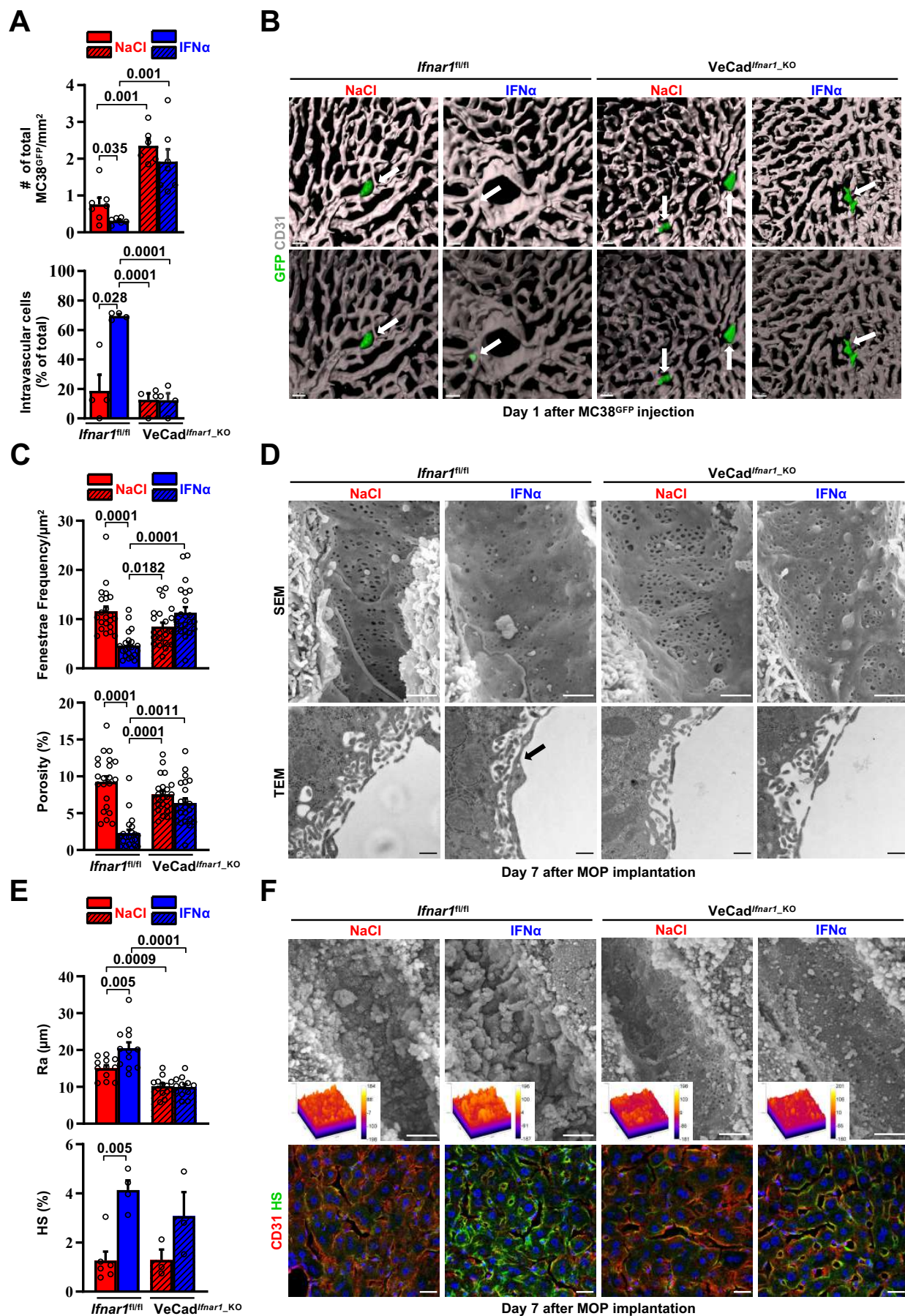


Figure 5. Continuous IFN α administration limits trans-sinusoidal migration of CRC cells by strengthening the hepatic vascular barrier. (A) Total number of MC38^{GFP} cells per area (top) and total number of intravascular MC38^{GFP} cells per tissue area (bottom). The total hepatic area was approximately

5mm² for each experimental group. Intravascular localization was measured on 20x images, 5 randomly selected images per mouse (n=3 per group). Mean values \pm SEM are shown; p-values were calculated by Mann-Whitney test. **(B)** Confocal reconstruction of the liver vasculature from *lfnar1^{fl/fl}* and *VeCad^{lfnar1-KO}* mice 24 hours after MC38^{GFP} cells (green) intramesenteric vein injection in mice that were treated with NaCl or IFN α for 7 days. CD31 is shown in grey. To allow visualization of intravascular MC38^{GFP} cells and to enhance image clarity, the transparency of the sinusoidal rendering was increased up to 80% (bottom). Scale bars=20 μ m. **(C)** Fenestrae frequency histogram (top) and percentage of vessel porosity (the percentage of liver endothelial surface area occupied by fenestrae, bottom) in liver sections of control *lfnar1^{fl/fl}* and *VeCad^{lfnar1-KO}* mice treated for 7 days with continuous NaCl or IFN α therapy. Quantification was performed on 17.000x SEM images, 10 randomly selected images per mouse (n=3 per group). A total area of approximately 720 μ m² of sinusoidal surface was analyzed for each mouse. Mean values \pm SEM are shown; p-values were calculated by Mann-Whitney test. **(D)** Representative scanning electron micrographs (SEM, top) and transmission electron micrographs (TEM, bottom) images from liver sections of mice described in **(C)**, showing hepatic fenestrations and endothelial features. Arrow indicates the increased endothelial thickness observed after continuous IFN α therapy in *lfnar1^{fl/fl}* mice. SEM scale bars=1 μ m; TEM scale bars=500nm. **(E)** Quantification of the arithmetical mean deviation or Ra coefficient (top) and the percentage of hepatic area positive for HS staining (bottom) on *lfnar1^{fl/fl}* and *VeCad^{lfnar1-KO}* livers treated with continuous NaCl or IFN α therapy for 7 days. Quantification was performed on at least 3 *lfnar1^{fl/fl}* and *VeCad^{lfnar1-KO}* livers per group. Mean values \pm SEM are shown; p-values were calculated by Mann-Whitney test. **(F)** Liver sinusoidal endothelial glycocalyx (GCX) visualization by scanning electron micrographs (SEM, top) from *lfnar1^{fl/fl}* and *VeCad^{lfnar1-KO}* livers that were perfused with lanthanum nitrate (a heavy metal that allows GCX visualization by stabilizing negatively charged GCX structures) 7 days after continuous NaCl or IFN α therapy. Scale bars=1 μ m. Inserts display a representation of the 3D topographic surface of a selected area within the liver sinusoid of each experimental condition. Representative immunofluorescence micrographs of Heparan sulfate (HS; green) and CD31 (red) staining from *lfnar1^{fl/fl}* and *VeCad^{lfnar1-KO}* mice treated with continuous NaCl or IFN α therapy for 7 days, showing increased HS accumulation after IFN α therapy only in *lfnar1^{fl/fl}* mice (bottom). Hoechst (blue) was used for nuclear counterstaining.

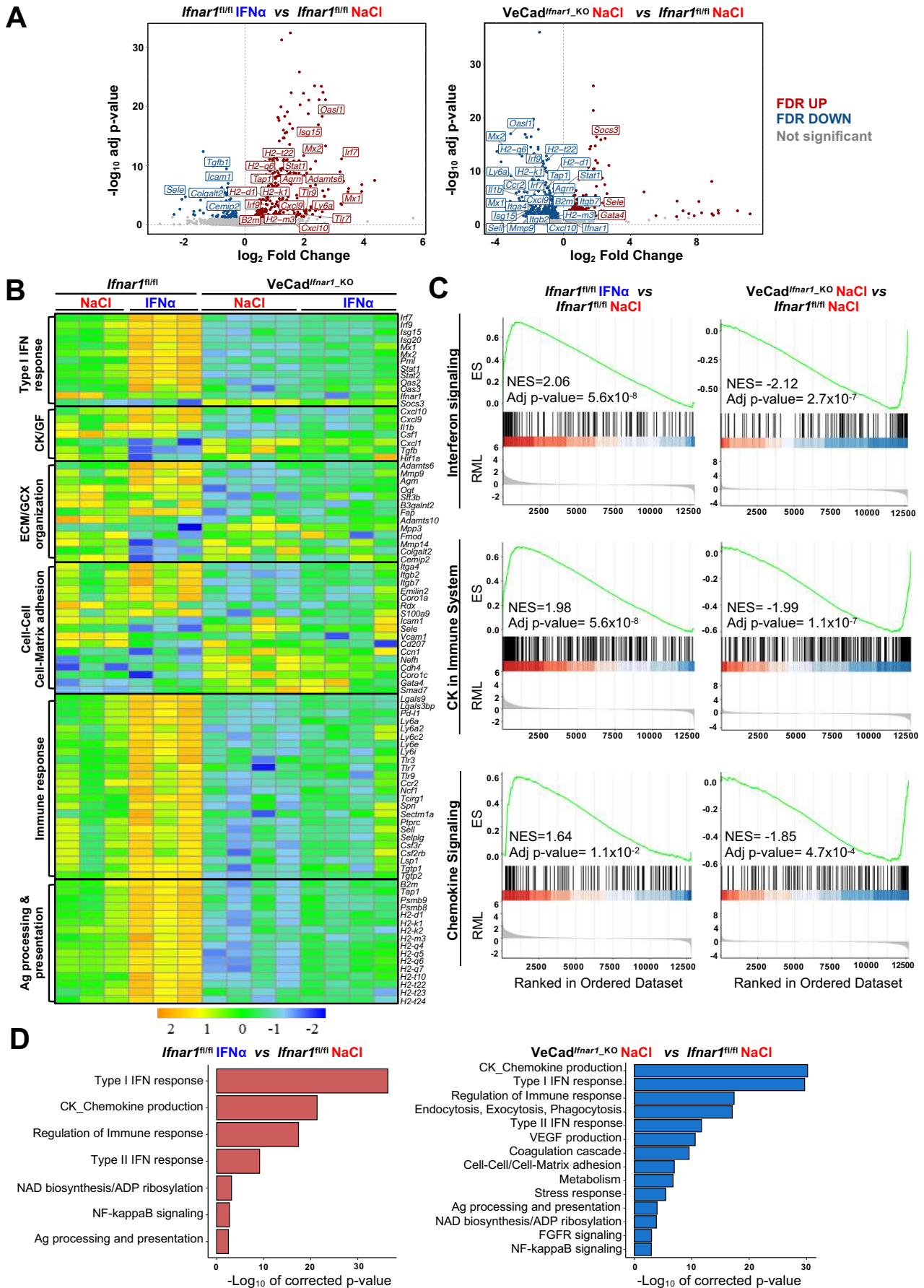


Figure 6. HECs acquire an antimetastatic transcriptional profile upon continuous IFN α sensing. (A) Volcano plots of differential gene expression (DGE) results obtained from the comparisons between HECs-derived from *Ifnar1^{fl/fl}* mice treated with NaCl and IFN α for 7 days (left) and between HECs-derived from

VeCad^{*Ifnar1*^{-KO}} and *Ifnar1*^{fl/fl} NaCl-treated mice (right) (*Ifnar1*^{fl/fl} n=3; VeCad^{*Ifnar1*^{-KO}} n=4). Significant false discovery rate (FDR<0.05) up- and down-regulated genes are highlighted in red and blue colors, respectively, not significant genes are depicted in grey. **(B)** Heatmap of the expression values (log2-transformed rpkm) of manually selected genes retrieved from differentially regulated pathways. **(C)** Pre-ranked Gene Set Enrichment Analysis (GSEA) enrichment plots of the indicated pathways between CD31⁺ cells from *Ifnar1*^{fl/fl}-IFN α and *Ifnar1*^{fl/fl}-NaCl (left) and between VeCad^{*Ifnar1*^{-KO}}-NaCl and *Ifnar1*^{fl/fl}-NaCl-treated animals (right). **(D)** Bar charts showing the adjusted p-values (-log10 transformed) of selected pathways from the enrichment analysis performed on comparisons between *Ifnar1*^{fl/fl}-IFN α and *Ifnar1*^{fl/fl}-NaCl CD31⁺ cells (left graph) and between VeCad^{*Ifnar1*^{-KO}}-NaCl and *Ifnar1*^{fl/fl}-NaCl CD31⁺ cells (right graph).

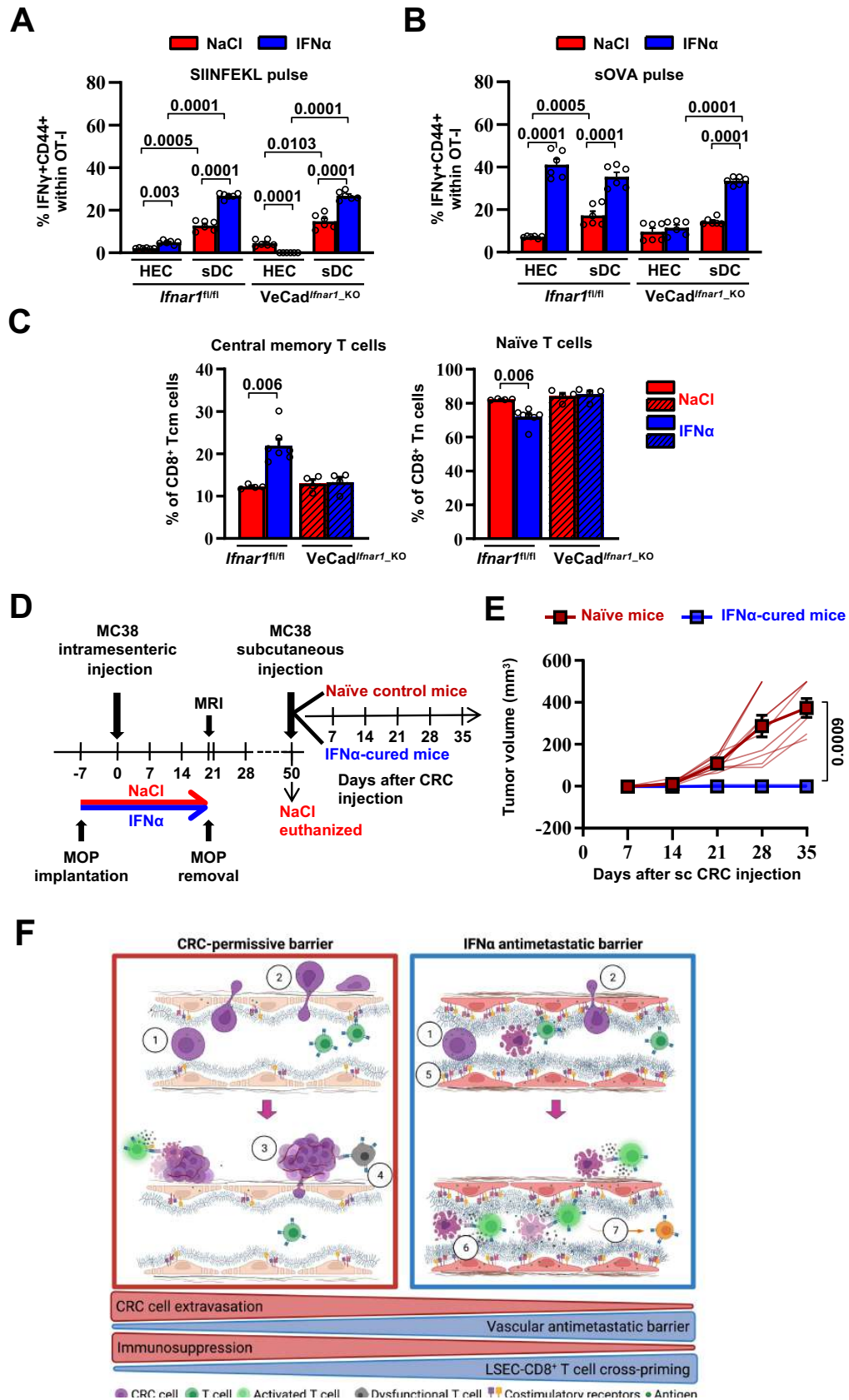


Figure 7. Continuous IFN α sensing improves immunostimulatory properties of HECs to provide long-term tumor protection. (A-B) Quantification of the percentage of OT-I CD8⁺ T cells expressing CD44⁺IFN γ ⁺ generated after the co-cultured with HECs, including LSECs, or sDCs isolated from *Ifnar1^{fl/fl}* and *VeCad^{Ifnar1-KO}* mice and stimulated with SIINFEKL peptide (A) or soluble OVA protein (sOVA) (B) in the presence of NaCl or IFN α . Mean values \pm SEM are shown; p-values were calculated by two-way ANOVA test from 2 independent experiments with 3 biological replicates each. (C) Quantification of the percentage of splenic T central memory (Tcm, CD8⁺CD44⁺CD62L⁺) and naïve T cells (Tn, CD8⁺CD44⁺CD62L⁺) populations 21 days after

intramesenteric MC38 cells injection into NaCl- or IFN α -treated *Ifnar1^{fl/fl}* and *VeCad^{Ifnar1-KO}* mice. Quantification was performed on least 4 mice per group. Mean values \pm SEM are shown; p-values were calculated by Mann-Whitney test. **(D)** Schematic representation of the experimental procedure used for tumor rechallenge. IFN α -*Ifnar1^{fl/fl}*-cured mice and naïve *Ifnar1^{fl/fl}* mice were subcutaneously rechallenged with 5×10^3 MC38 cells and received no further treatment. Tumor growth was monitored weekly for 35 days. Note that we used aged-matched *Ifnar1^{fl/fl}* naïve mice because NaCl-treated mice had to be euthanized for ethical reasons by day 50. **(E)** Kinetics of subcutaneous tumor growth in naïve (n=10) and IFN α -cured (n=7) mice. Both, mean tumor volume and individual animal measurements are shown. Mean values \pm SEM are shown; p-values were calculated by two-way ANOVA test. **(F)** Schematic model: CRC cells emerging from the primary tumor reach the hepatic sinusoids via the portal circulation and arrest - mostly because of size constrains - at the portal side of the sinusoidal circulation (1), CRC cells trans-sinusoidally migrate into the liver parenchyma (2) and develop micro-metastases that will eventually grow overtime (3; red frame), promoting the generation of an immunosuppressive microenvironment leading to dysfunctional T cells (4; red frame). Conversely, IFN α therapy (blue frame), by modifying LSECs porosity, thickness, deposition of basal membrane and GCX depth, builds up a vascular antimetastatic barrier (5), that impairs CRC trans-sinusoidal migration, promoting intravascular containment of invading tumor cells (6) that together with IFN α -mediated increased cross-presentation and cross-priming by HECs/LSEC, will lead to naïve CD8⁺ T cell activation and secondary generation of long-term antitumor immunity and protection from secondary tumor challenge (7). Created with BioRender.com.